PHYSICAL REVIEW D **69**, 124036 (2004)

Mergers of irrotational neutron star binaries in conformally flat gravity

Joshua A. Faber, Philippe Grandclément,* and Frederic A. Rasio
Department of Physics and Astronomy, Northwestern University, Evanston, Illinois 60208, USA

(Received 21 December 2003; revised manuscript received 12 April 2004; published 30 June 2004)

We present the first results from our new general relativistic, Lagrangian hydrodynamics code, which treats gravity in the conformally flat (CF) limit. The evolution of fluid configurations is described using smoothed particle hydrodynamics (SPH), and the elliptic field equations of the CF formalism are solved using spectral methods in spherical coordinates. The code was tested on models for which the CF limit is exact, finding good agreement with the classical Oppenheimer-Volkov solution for a relativistic static spherical star as well as the exact semianalytic solution for a collapsing spherical dust cloud. By computing the evolution of quasiequilibrium neutron star binary configurations in the absence of gravitational radiation back reaction, we have confirmed that these configurations can remain dynamically stable all the way to the development of a cusp. With an approximate treatment of radiation reaction, we have calculated the complete merger of an irrotational binary configuration from the innermost point on an equilibrium sequence through merger and remnant formation and ringdown, finding good agreement with previous relativistic calculations. In particular, we find that mass loss is highly suppressed by relativistic effects, but that, for a reasonably stiff neutron star equation of state, the remnant is initially stable against gravitational collapse because of its strong differential rotation. The gravity wave signal derived from our numerical calculation has an energy spectrum which matches extremely well with estimates based solely on quasiequilibrium results, deviating from the Newtonian power-law form at frequencies below 1 kHz, i.e., within the reach of advanced interferometric detectors.

DOI: 10.1103/PhysRevD.69.124036 PACS number(s): 04.30.Db, 47.11.+j, 95.85.Sz, 97.60.Jd

I. INTRODUCTION

Gravitational wave (GW) astronomy stands at a crucial moment in its history, with the LIGO (Laser Interferometer Gravitational Wave Observatory) Scientific Collaboration reporting results from their first scientific runs [1–3], GEO600 having completed two scientific runs [4,5], TAMA taking data [6,7], and VIRGO reporting its first lock acquisition [8–10]. As such, it is now more important than ever to have accurate theoretical predictions of the main candidate signals, both to aid in their detection and to facilitate the interpretation of any future detections.

It has long been recognized that coalescing relativistic binary systems containing compact objects, either neutron stars (NS) or black holes (BH), are likely to be important sources of detectable GWs. Recent population synthesis calculations indicate that an Advanced LIGO detector should be able to see at least tens of coalescences per year of NS-NS, NS-BH, and BH-BH binaries [11]. Empirical rate estimates based on three of the four observed binary pulsar systems expected to merge within a Hubble time, PSR B1913+16, PSR B1534+12, and PSR J0737-3039 [12], are in general agreement, with the latter making the dominant contribution to the probabilistic rate because of its short coalescence time of 85 Myr (see [13,14] and references therein; the fourth system is located in a globular cluster, rather than the galactic plane). NS-NS binaries are the only known systems with coalescence times shorter than a Hubble time to have been conclusively observed, and it is the orbital decay of PSR1913+16 that currently provides our best indirect evidence for the existence of GWs [15–17].

At large separations, the dynamics of compact object binaries can be well approximated by high-order post-Newtonian (PN) (see [18] and references therein) and other formalisms [19,20] which treat the compact objects as point-masses, including the effects of spin-orbit and spin-spin angular momentum couplings for systems containing a BH [21–23]. In general, these methods are more appropriate for describing a BH than a NS, since the finite-size effects ignored by point-mass formulas are of greater magnitude in systems containing NS.

For smaller binary separations, $r \lesssim 10 R_{NS}$, where R_{NS} is the radius of the NS, these finite-size corrections play an increasingly significant role in the evolution of NS-NS binaries. As long as the coalescence time scale $\tau = r/\dot{r}$ remains longer than the dynamical time scale, the evolution is quasiadiabatic, and the binary will sweep through a sequence of configurations representing energy minima for given binary separations. The infall rate will be given by

$$\frac{dr}{dt} = \left(\frac{dE}{dt}\right)_{GW} \left(\frac{dE(r)}{dr}\right)_{eq}^{-1}, \tag{1}$$

where $(dE/dt)_{GW}$ is the energy loss rate to gravitational radiation, and $(dE/dr)_{eq}$ is the slope of the equilibrium energy curve. Equilibrium energy sequences were first constructed in Newtonian and then PN gravity (see [24] and references therein). More recently, general relativistic (GR) sequences have been calculated for binary NS systems in quasicircular orbits [25–32]. An important result from these studies is that the slope of the equilibrium energy curve is flatter when relativistic effects are included, compared to the Newtonian

---

*Current address: Laboratoire de Mathématiques et de Physique Théorique, Université de Tours, Parc de Grandmont, 37200 Tours, France.

value. This becomes especially pronounced at small separations, near the point where equilibrium sequences encounter an energy minimum (often associated with the "innermost stable circular orbit," or ISCO) or terminate when a cusp develops on the inner edge of the NS. Based on this observation, it was noted that a flatter slope in the equilibrium energy curve results in not only a faster infall rate but also a decrease in the energy spectrum, $dE/df \approx (dE/dr)/(df/dr)$. In fact, based on the relativistic equilibrium sequences of Taniguchi and Gourgoulhon ([27], hereafter TG), Faber *et al.* ([33], hereafter FGRT) concluded that the dependence of finite-size corrections on the NS compactness (i.e., M_{NS}/R_{NS}) would leave an imprint in the GW energy spectrum at frequencies $f\approx 500$–1000 Hz, within the band accessible to Advanced LIGO. Hughes [34] proposed a method using these results which would allow for a determination of the NS compactness to within a few percent based on 10–50 observations with Advanced LIGO if it employs a narrow-band detector in addition to the current broadband setup, with the required number of observations dependent upon both the true compactness and the particular setup of the detector.

Shortly before the ISCO or the end of the equilibrium sequence (when it terminates at the formation of a cusp) the binary will begin a transition toward a rapid plunge inward, eventually leading to merger. Once the binary passes this point, the dynamical evolution becomes too complicated to describe using semianalytical methods, requiring instead a 3D hydrodynamic treatment. Such calculations were performed first for Newtonian gravitation, using both Eulerian, grid-based codes and Lagrangian smoothed particle hydrodynamics (SPH; for a review, see, e.g., [35] and references therein). It was always recognized that any results would be at best qualitatively accurate, since the extreme compactness of the NS would induce a host of GR effects. Noting this, some attempts were made to calculate the evolution of binary NS systems in lowest-order PN gravity [35–39], using a formalism developed by [40]. Unfortunately, using realistic NS equations of state (EOS) violated the basic assumption of the PN approximation that the magnitude of the 1PN terms are small relative to Newtonian-order effects. As a result, all PN calculations were forced to make unphysical approximations, either by evolving NS with a fraction of their proper physical mass [38,39], or by reducing the magnitude of all 1PN terms [[35–37], hereafter denoted FR1-3, or collectively FR].

While the ultimate goal of studying binary NS coalescences should be a full GR treatment, only one group has been able to calculate the full evolution of a binary system from an equilibrium binary configuration through merger and the formation of a remnant [41–43]. While these calculations represent a breakthrough in our understanding of the hydrodynamics of coalescing NS binaries, they still leave a great deal of room for further research into a variety of questions. Currently, full GR calculations are extremely difficult, and are vulnerable to several numerical instabilities. In order to guarantee the stability of calculation through coalescence and the formation of either a stable merger remnant or a BH, binaries were started from the termination points of equilibrium sequences, from quasicircular configurations with zero infall velocity. The calculations of Shibata and Uryu [41,42] used initial conditions generated by Uryu, Eriguchi, and collaborators [31,32], and the more recent work by Shibata, Taniguchi, and Uryu [43] used initial conditions generated by TG. This restricts studying the behavior of the infall velocity and GW signal when the stars begin their plunge, during which time detected signals may yield important information, as mentioned above. The lack of information about the dynamics of binaries before the plunge also hinders testing the validity of the initial matter and field configurations used in full GR calculations. While the assumptions defining the quasiequilibrium configuration are certainly reasonable, it is difficult to gauge how well such configurations agree with those evolved dynamically from larger separations. Also unknown in detail is the effect that errors in the initial configuration will have on the system as they propagate in nonlinear fashion during the calculation.

A further technical difficulty with full GR calculations results from computational limits, since numerical grids are currently constrained to have their boundaries lie within approximately half of a GW wavelength, within the near zone. This can induce possibly significant errors into the GW extraction process, which would ideally be performed by studying the behavior of the metric in the wave zone.

A possible middle road, at least at present, is provided by the conformally flat (CF) approximation to GR, first described by Isenberg [44] and developed in greater detail by Wilson and collaborators [45] (note that their original version contained a mathematical error, pointed out by Flanagan [46], accounting for spurious results with regard to "crushing" effects on NS prior to merger). This formalism includes much of the nonlinearity inherent in GR, but yields a set of coupled, nonlinear, elliptic field equations, which can be evolved stably. The first dynamical 3D calculations to make use of the CF framework were performed by Shibata, Baumgarte, and Shapiro [47], who created a PN variant by discarding some of the nonlinear source terms in the field equations while retaining the vast majority of the nonlinearity in the system. They found, among other things, that the maximum density of the NS is smaller for binary configurations than in isolation, and that NS in binaries have a higher maximum mass as well, strongly indicating that collapse to a BH prior to merger is essentially impossible. The first calculations to use the full formalism were performed by Oechslin *et al.* [48], using a Lagrangian SPH code with a multigrid field solver. Using corotating initial configurations, which are thought to be unphysical (since viscous effects are thought to be much too weak to tidally synchronize the NS [49,50]), they found that mass loss during the merger is suppressed in relativistic gravitational schemes, as had been previously suggested based on calculations in PN gravity (FR3).

While the CF formalism appears to be safer than full GR with regard to evolving the system stably, the grid-based approaches used so far suffer from many of the same problems faced by full GR calculations. Since the CF field equations are nonlinear and lack compact support, approximate boundary conditions for the fields must be applied at the boundary of the grid, which can lead to errors in the solution. Additionally, very large grids are required to satisfy the tradeoff between large grid sizes, required to improve the accuracy of the boundary conditions, and small grid cell sizes, necessary to improve the resolution of the NS. Multigrid techniques can be very valuable for such cases, but grid refinement techniques can also act as a source of numerical errors. Noting this, we have taken an entirely new approach to the dynamical evolution of binary NS systems with SPH, which requires no use of rectangular 3D grids to solve for the metric fields. Instead, we use the LORENE numerical libraries, developed by the Meudon group, which are freely available online[1] (see [51], hereafter BGM, and [52] for a thorough description of the numerical techniques used in LORENE). These routines, which use spectral methods and iterative techniques to solve systems of coupled nonlinear multidimensional PDEs, have been used widely to study quasiequilibrium sequences of binary NS systems in Newtonian [53,54] and CF gravity (TG [26,55]), as well as a number of other fluid configurations. The CF quasiequilibrium solutions of Gourgoulhon *et al.* [26] and TG have been used as the initial configurations for the most recent full GR calculations of Shibata, Taniguchi, and Uryu, [43], and will be used in this work as well.

Our work here represents the first time that spherical coordinates and spectral methods have been used to study the dynamical evolution of binary NS systems in any gravitational formalism, including Newtonian gravity. It has long been known that these techniques are ideal for describing both binary systems with large separations as well as the merger remnants formed during the coalescence, since the spherical coordinates correspond much more naturally to the metric fields than rectangular coordinates can. Traditionally, rectangular grids have been used anyway, both because they are more widespread throughout computational fluid dynamics, but also because they are viewed as more robust. It has often been assumed that spherical coordinate field solvers may fail to calculate fields properly during the merger, when the matter can be described neither as two spheroids nor as one, but rather some combination of the two, with mass loss streams and other phenomena confusing the picture. We show here, however, that spectral methods can be used successfully in this regime, taking advantage of the multidomain techniques of LORENE. This allows us to take advantage of the many advantages inherent to spectral methods: improved speed, vastly improved computer memory efficiency, and a coordinate system which allows for a natural treatment of the exact boundary conditions.

The code we have developed to perform 3D, relativistic, numerical hydrodynamic evolutions is well-suited for the study of a number of physical systems. While we focus here on merging binary NS, our code is capable of evolving essentially any binary or single-body relativistic fluid configuration. These include collapsing stellar cores and supermassive stars, and rapidly rotating fluid configurations. Modules currently exist to handle a number of physically-motivated EOS, including models with phase transitions and bosonic condensates, and we plan to extend our studies to include appropriate treatments of these conditions in the future.

Our paper is structured as follows. In Sec. II, we summarize the theoretical basis for our new relativistic Lagrangian code, describing in turn the numerical methods used to implement both the dynamical equations of the CF formalism in SPH and the details of our spectral methods field solver. In Sec. III, we turn to the computational aspects of the code relevant to coalescing binary systems. We detail the choices we have made with regard to SPH discretization, the techniques used to convert between particle-based and spectrally decomposed descriptions of various quantities, and the coordinate transformations implemented to describe binary systems, merging systems, and the resulting remnants. In Sec. IV, we report the results of several test calculations, including two well-known exact CF solutions as well as the evolution of quasiequilibrium configurations in the absence of dissipative effects, producing circular orbits. In Sec. V, we show our results from the calculation of a full NS binary coalescence started from the innermost quasiequilibrium configuration, and followed through the merger and the formation of a merger remnant. We compare our results to previous work in the field, including full GR calculations using the same initial condition. Finally, in Sec. VI, we summarize our results and lay out some of the many classes of problems in relativistic hydrodynamics where our code may prove useful.

II. NUMERICAL METHODS

The CF approximation assumes that the spatial part of the GR metric is equal to the flat-space form, multiplied by a conformal factor which varies with space and time. Setting $G=c=1$, as we will do throughout this paper, the CF metric takes the form

$$ds^2=-(N^2-N_iN^i)dt^2-2N_i dt dx^i+A^2 f_{ij} dx^i dx^j, \quad (2)$$

where N is the lapse function, N_i is the shift vector, and A will be referred to here as the conformal factor (see Table I for a comparison of our notation to those of [26,45,47,48], which are all based on the same exact assumptions). The flat-space three-metric is denoted by f_{ij}. We follow the standard notation for relativistic tensors, denoting spatial three-vectors with Latin indices, and relativistic four-vectors with Greek indices. While the CF approximation cannot reproduce the exact GR solution for an arbitrary matter configuration, it is exact for spherically symmetric systems, and yields field solutions which agree with those calculated using full GR to within a few percent for many systems of interest [56].

As is typical for any relativistic calculation utilizing a polytropic EOS, there is a single physical scale which defines the units for the problem. We choose to define this scale for single-body test calculations (Secs. IV A and IV B) by dividing all mass, length, and time-based quantities by the gravitational (ADM) mass M_0 of the object. For all binary calculations, we scale our results by the ‘‘chirp mass’’ of the system, $\mathcal{M}_{ch} \equiv \mu^{3/5} M_t^{2/5}$, where M_t is the total gravitational mass of the system at large separation, and $\mu \equiv M_1 M_2 / M_t$ is the reduced (gravitational) mass. This quantity is expected to be the most directly measurable physical parameter deduced from any GW observation (see, e.g., [57]). For a binary sys-

---

[1] http://www.lorene.obspm.fr

TABLE I. A comparison of our notation for various relativistic quantities to previous works using the CF formalism: [26,45,47,48]. For those cases where no unique terminology was defined, we give the simplest equivalent algebraic form. We also list the equation in this paper where the quantity is defined.

Quantity	Here	Gourgoulhon	Oechslin	Shibata	Wilson	See Eq.
Lapse	N	N	α	α	α	(2)
Shift	N_i	N_i	$-\beta_i$	$-\beta_i$	$-\beta_i$	(2)
Conf. Fact.	A	A	ψ^2	ψ^2	ϕ^2	(2)
Rest dens.	ρ_*	$\Gamma_n A^3\rho$	ρ_*	ρ_*	$D\phi^6$	(5)
Lorentz Fact.	γ_n	Γ_n	αu^0	αu^0	W	(6)
Velocity	v^i	NU^i+N^i	v^i	v^i	V^i	(7)
Spec. Momentum	$\tilde{u}_i$	w_i	$\tilde{u}_i$	$\tilde{u}_i$	$S_i/(D\phi^6)$	(10)
Enthalpy	h	h	w	$1+\Gamma\epsilon$	h	(11)

tem consisting of two $M_0=1.4\ M_\odot$ NS, the chirp mass is $\mathcal{M}_{ch}=1.22\ M_\odot$, which yields characteristic distance and time scales $R=1.80$ km and $T=6.00\times10^{-6}$ sec, respectively. To compare our results with the equivalent relativistic model (run M1414) of [43], who use the total gravitational mass of the binary at large separation as their unit, one can divide our quoted masses and radii by a factor of $2^{1.2}=2.30$. To convert our time evolution results into the time units used in [43], which are defined in terms of the initial binary orbital period, divide our time units by a factor of 443 (their unit $P_{t=0}=2.66$ ms for two NS each with $M_0=1.4\ M_\odot$).

A. CF smoothed particle hydrodynamics

In what follows, we will assume that the stress-energy tensor of the fluid is that of a perfect fluid, with

$$T_{\mu\nu}=(\rho+\rho\epsilon+P)u_\mu u_\nu+Pg_{\mu\nu}, \tag{3}$$

where ρ is the rest-mass density, ϵ is the specific internal energy, P the fluid pressure, and u_μ the four-velocity of the fluid. For our initial data, we assume a polytropic EOS $P=k\rho^\Gamma$, with constant values for k and the adiabatic index Γ, and throughout the calculation we assume that the evolution is adiabatic, such that $P=(\Gamma-1)\rho\epsilon$. The maximum infall velocity of the two stars relative to each other during our dynamical calculations was found to be $v_{in}=0.06$c, whereas the sound speed at the center of the NS is initially $c_s=0.85$c. Since the sound speed for our EOS depends on density such that $c_s\propto\rho^{1/2}$, we expect that the only supersonic fluid flows will occur in the very tenuous outer regions of the NS. During the merger, we do expect that low-density matter from the inner edge of each NS will cross over to the binary companion at high relative velocity ($\delta v\approx0.3$c), but the velocity field is dominated by the circular motion, rather than a converging flow. All motion within the cores of the NS should remain strongly subsonic throughout the merger process.

Using our CF metric and stress-energy tensor, Eqs. (2) and (3), the Lagrangian continuity equation is given by

$$\frac{d\rho_*}{dt}+\rho_*\nabla_i v^i=0, \tag{4}$$

where the rest mass density is defined by

$$\rho_*\equiv Nu^0A^3\rho=\gamma_n A^3\rho, \tag{5}$$

the Lorentz factor of the fluid is defined as

$$\gamma_n\equiv Nu^0, \tag{6}$$

and the physical velocity is given by

$$v^i\equiv u^i/u^0=N^i+\frac{u_i}{A^2u^0}. \tag{7}$$

Note that u^0 is the timelike element of the covariant 4-velocity; all other numerical superscripts refer to exponents. Following the SPH prescription, this conservative form of the continuity equation allows us to define a set of particles, each of which has a fixed mass m_a and a well defined velocity given by $dx_i/dt=v_i$. For each particle "a," we also define a "smoothing length," h_a, which represents the physical size of the particle. SPH particles do not have delta-function density profiles; rather, each particle represents a spherically symmetric density distribution centered at the particle's position $\vec{x}_a$ with compact support. This density distribution, determined by our chosen form of the smoothing kernel function, is second-order differentiable, and drops to zero at a radius equal to two smoothing lengths from the particle's position. For each particle, we define a set of neighboring particles by the condition that all particles whose centers fall within a given particle's compactly supported density distribution are its neighbors. To determine the proper smoothing length for each particle, we define an ideal number of neighbors for each particle, N_N, and we use a relaxation technique to adjust h_a after every time step (as described in detail in, e.g., FR1 and [58]). We note in passing that "neighborhood" is not a reflexive property; we handle this through the use of a "gather-scatter" algorithm (see [59] for details).

The primary advantage of the SPH method over traditional grid-based codes is that fluid advection is handled in a natural way, such that one can define the edge of a fluid distribution without recourse to artificial "atmospheres" or other tricks necessary to prevent matter from bleeding into the vacuum. Particles simply follow their trajectories in the fluid flow. As such, SPH is extremely computationally efficient, since all numerical resources are focused automatically on those regions containing matter. Because of this, SPH also allows for high spatial resolution. The primary disadvantage of SPH compared to shock-capturing grid-based codes is in the lower resolution of shock fronts, which, as we discuss below, is unimportant here.

All hydrodynamic quantities can be defined using standard SPH summation techniques over each particle's neighbor list (see, e.g., [58,60,61] for a thorough discussion), with the rest mass density ρ_* taking the place of the standard Newtonian density. Thus the rest-mass density for particle "a" can be defined via SPH summation over a set of neighboring particles denoted by "b" as

$$(\rho_*)_a = \sum_b m_b W_{ab}, \tag{8}$$

where W_{ab} is the W_4 smoothing kernel function for a pair of particles first introduced by Monaghan and Lattanzio [62], used in FR, [58] and many other implementations. The momentum equation is given by

$$\frac{d\tilde{u}_i}{dt} = -\frac{NA^3}{\rho_*}\nabla_i P - Nhu^0\nabla_i N - \tilde{u}_j\nabla_i N^j + \frac{\tilde{u}_k\tilde{u}_k}{A^3hu^0}\nabla_i A, \tag{9}$$

where the specific momentum is defined by

$$\tilde{u}_i \equiv hu_i, \tag{10}$$

and the specific enthalpy is defined as

$$h \equiv (1+\epsilon+P/\rho) = 1+\Gamma\epsilon. \tag{11}$$

In this expression and throughout this paper, covariant derivatives are associated with the flat-space metric. In the absence of nonadiabatic artificial viscosity terms, the energy equation merely implies that the value of k in the EOS remains constant. In our calculation, we use ρ_* and $\tilde{u}_i$ as the basic hydrodynamic variables (in addition to our uniform value of k). To find u^0, which enters into the momentum equation, we take the normalization condition for the 4-velocity, $u_\mu u^\mu = -1$, and find

$$\gamma_n^2 = (Nu^0)^2 = 1 + \frac{u_i u_i}{A^2} = 1 + \frac{\tilde{u}_i\tilde{u}_i}{A^2}\left[1 + \frac{\Gamma k \rho_*^{\Gamma-1}}{(\gamma_n A^3)^{\Gamma-1}}\right]^{-2}, \tag{12}$$

which can be solved implicitly in terms of the density and the field values.

To solve the field equations of GR, we need to fix the slicing condition for timelike hypersurfaces. Following the standard approach to the CF formalism, we find that the extrinsic curvature tensor is given in terms of the shift vector as

$$K^{ij} \equiv \frac{1}{2NA^2}\left(\nabla^i N^j + \nabla^j N^i - \frac{2}{3}f^{ij}\nabla_k N^k\right), \tag{13}$$

when we assume the maximal slicing condition ($\mathrm{Tr}\,K=0$). To lower the indices of the extrinsic curvature tensor and other spatially-defined quantities, we use the conformal flat-space metric (i.e., $K_{ij} = A^4\delta_{ik}\delta_{jl}K^{kl}$ in Cartesian coordinates, where δ_{ij} is the Cartesian flat-space metric). Combining the maximal slicing assumption with the Hamiltonian constraint yields a pair of elliptic equations for $\nu \equiv \ln(N)$ and $\beta \equiv \ln(AN)$ (GGTMB), in the form

$$\nabla_k\nabla^k\nu = 4\pi GA^2(E+S) + A^2K_{ij}K^{ij} - \nabla_i\nu\nabla^i\beta, \tag{14}$$

$$\nabla_k\nabla^k\beta = 4\pi GA^2S + \frac{3}{4}A^2K_{ij}K^{ij} - \frac{1}{2}(\nabla_i\nu\nabla^i\nu + \nabla_i\beta\nabla^i\beta), \tag{15}$$

where the matter energy density and the trace of the stress energy tensor are given by

$$E \equiv \gamma_n^2(\rho h) - P, \tag{16}$$

$$S \equiv \frac{\gamma_n^2 - 1}{\gamma_n^2}(E+P) + 3P. \tag{17}$$

Note that Eqs. (14) and (15) are algebraically equivalent to the field equations found in other papers on the CF formalism, although most groups have typically solved the corresponding Poisson-type equations for $\psi \equiv \sqrt{A}$ and $N\psi$. Finally, the momentum constraint gives us the equation for the shift vector,

$$\nabla^j\nabla_j N^i + \frac{1}{3}\nabla^i\nabla_j N^j = -16\pi G\frac{N}{h\gamma_n}(E+P)\tilde{u}_i + 2NA^2K^{ij}\nabla_j(3\beta - 4\nu). \tag{18}$$

Since the CF formalism is time-symmetric, we can define several conserved quantities. The total baryonic mass,

$$M_b = \int \rho_* d^3x, \tag{19}$$

is automatically conserved in our SPH scheme, since we use the rest mass density to define particle masses. The total angular momentum of the system can be defined as

$$J_i = \varepsilon_{ijk}\int \rho_* x^j \tilde{u}_k d^3x. \tag{20}$$

Finally, the ADM mass is given by

$$M_0 = \int \rho_{ADM} d^3x; \qquad \rho_{ADM} \equiv A^{5/2}\left(E + \frac{1}{16\pi G}K_{ij}K^{ij}\right). \tag{21}$$

It is important for numerical reasons to note that the two terms that make up the ADM mass density ρ_{ADM} have different behaviors: the contribution from the matter energy density,

$$\rho_1 \equiv A^{5/2}E, \tag{22}$$

has compact support, and is nonzero only in the presence of matter, whereas the term involving the extrinsic curvature,

$$\rho_2 \equiv \frac{1}{16\pi G} A^{5/2} K^{ij} K_{ij}, \tag{23}$$

extends throughout all space with power-law fall-off at large radii.

B. The spectral methods field solver

The spectral methods techniques we use to solve the CF field equations, Eqs. (14), (15) and (18), discussed in great detail in [52], provide a number of important advantages not present in traditional grid-based approaches. First and foremost is their speed and computational efficiency. Finite differencing schemes typically require 3D grid sizes of $\gtrsim 10^6$ elements [43,48]. In contrast, GGTMB show that spectral method field solvers can be used to construct field solutions yielding ADM masses and angular momenta convergent to within 10^{-4} and satisfying the virial theorem to the same level using only 3 grids of size $17\times 13\times 12$. These grids, extremely small compared to those used in Cartesian multigrid solvers, result in a great increase in speed. Additionally, the use of spherical coordinates allows for a more natural treatment of boundary conditions. In the approach we use, taken from GGTMB and summarized here, space is described using spherical coordinates, split into a set of nested "computational domains." The outermost domain can be compactified by rewriting the field equations in terms of $1/r$, allowing us to impose the exact boundary conditions at infinity, rather than "fall-off" boundary conditions which approximate the behavior of the fields at the edges of a rectangular grid. As such, we avoid the classic tradeoff between a grid with large grid spacing, which yields accurate boundary conditions but poor spatial resolution of the matter source, and a grid with small spacing, and the opposite concerns.

Combining the LORENE methods with particle-based SPH requires some small but significant changes from the previous approach described in detail in Sec. IV A of GGTMB. As in that work, we construct a set of three computational domains around each star to evaluate the field equations. The innermost domain has a spheroidal topology, with a boundary roughly corresponding to the SPH particle configuration's surface, as described in Sec. III A. The other two domains cover successively larger regions in radii, with the outermost domain extending out to spatial infinity, as shown in Fig. 1. The field equations are solved in each domain and the global solution is obtained by matching the function and its first radial derivative at each boundary. Appropriate boundary conditions at radial infinity are also imposed. All fields can be described in one of two complementary representations, either in terms of their coefficients in the spectral decomposition, or by means of their values at a set of "collocation points." The coordinate representations for these points are defined such that the origin of the system describing each NS is located at the position of the star's maximum density, The collocation points are spaced equally in both $\sin\theta$ and ϕ, as required by the angular component of the spectral decomposition. The radii of the points are determined from the collocation points of the Chebyshev polynomial expansion used for the radial coordinate, as described in BGM and GGTMB. For all calculations described in this paper, these domains consisted of a $17\times 13\times 12$ grid, in terms of radial, latitudinal, and longitudinal directions, respectively, an acceptable trade-off between speed and accuracy, based on the description above.

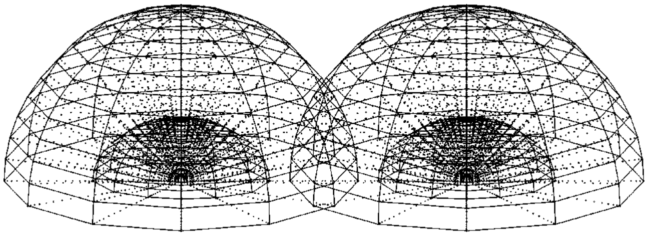

FIG. 1. Radial domains used to evaluate the field equations of the CF method. The boundaries of the inner two domains are shown as lattices, with all collocation points within these domains shown as well. The outermost domain, which extends to spatial infinity, is not shown.

A key feature of the LORENE libraries is their handling of binary systems in a straightforward and natural way. This involves "splitting" the source terms of the field equations into two distinct components, each of which is centered on one of the stars in the binary. Since the field equations in this case are nonlinear the split cannot be performed uniquely; the fields present around one star cannot be determined from its source terms only. Rather, this method seeks to minimize the contribution of one star to the fields around the other. In practice, both field variables and hydrodynamic source terms can be broken down, as shown in Eqs. (79)–(87) of GGTMB, such that

$$\nu = \nu_{\langle 1\rangle} + \nu_{\langle 2\rangle} = \nu_{\langle 1\rangle} + \nu_{\langle 2\to 1\rangle} = \nu_{\langle 1\to 2\rangle} + \nu_{\langle 2\rangle}, \quad \text{etc.} \tag{24}$$

where quantities labeled $\langle 1\rangle$ and $\langle 2\to 1\rangle$ are defined at the collocation points of star 1, and $\langle 2\rangle$ and $\langle 1\to 2\rangle$ at those of star 2. The autopotentials of each star, $\nu_{\langle 1\rangle}$ and $\nu_{\langle 2\rangle}$, are primarily generated by matter from the star itself, while the "comp-potentials," $\nu_{\langle 2\to 1\rangle}$ and $\nu_{\langle 1\to 2\rangle}$ are primarily generated by the other star. It is this conversion of fields between the two sets of coordinates which represents the greatest amount of numerical effort during a calculation. In practice, we attempt to minimize the magnitude of the comp-potentials since they are centered around the other star and not as well described by spherical coordinates. The detailed description of how these quantities are defined and calculated can be found in Sec. IV C of GGTMB.

III. NUMERICAL TECHNIQUES FOR COALESCING BINARIES

Integrating the LORENE library routines into an SPH-based Lagrangian code introduces a number of rather subtle numerical issues. The simplest of these is deciding the shape of the innermost computational domain's surface. The closer the boundary of the innermost domain lies to the surface of the fluid, the more Gibbs effect errors are minimized, so long as the surface is sufficiently smooth and convex everywhere. Gibbs effects, which are common to all spectral decomposition techniques, result from the attempt to describe a nondifferentiable density distribution as a weighted sum of smooth functions; they are relevant here when we attempt a spectral decomposition of a region of space where the density drops to zero within the boundary (see BGM for more details). Unfortunately, the smoothness and convexity conditions do not necessarily apply to the region in space where the SPH density is nonzero, since a single SPH particle being shed from the star can greatly affect the nonzero density boundary, even though it may represent an insignificant amount of mass. As a result, we have implemented an algorithm that attempts to take the middle ground, defining a boundary for the innermost domain which encloses as much of the mass as possible, in such a way that smoothness and convexity are guaranteed. The second domain is bounded by a sphere of radius twice that of the outermost point of the first domain, and a third domain extends to spatial infinity.

Once the configuration of the computational domains is determined, there are several choices which need to be made with regard to the most accurate and efficient way to calculate various terms in the evolution equations. Some hydrodynamic quantities, such as the rest mass density ρ_*, need to be defined for each of the SPH particles. Here, we use $N \sim 100\,000$ SPH particles for each run, which was found to be sufficient for achieving numerical convergence of the GW signal to the $\sim 1-2\,\%$ level in our studies with post-Newtonian SPH [35]. Other quantities, such as those appearing in the source terms for the field equations, need to be defined at every point among the $17\times 13\times 12$ spheroidal grids of collocation points for each of the three domains. Compared to solutions computed using larger grid sizes, we find that these agree with significantly larger grids to within $\sim 0.1\%$ for the value of the shift vector, and even better for the values of the lapse function and conformal factor.

In general, however, many quantities do not need to be defined both ways, so long as a full set of thermodynamic variables is known in both representations. Details about which quantities are used in each representation are given below. Briefly, it is most efficient to perform the majority of our algebraic operations on quantities defined at collocation points, reading in and exporting back as small a set of parameters as possible to the full set of SPH particles. While reading quantities from SPH particles to collocation points is relatively quick, requiring an SPH summation at every collocation point position, the reverse process is much more involved. To calculate the value of a quantity known in the spectral representation at SPH particle positions requires performing a sum over all spectral coefficients with the weights appropriate to each particle position, consuming a great deal of time.

A. Binary systems

To construct the initial SPH particle configuration for a binary NS evolution, we use the quasiequilibrium irrotational models of TG, which are publicly available.[2] These models describe the complete 3-dimensional structure of both the field values and hydrodynamic quantities at every point in space, in terms of a spectral decomposition. Specifically, we take the results of their irrotational run for stars of equal mass and equal compactness $GM/Rc^2=0.14$ with a $\Gamma=2$ polytropic EOS. Each star has a baryonic mass in isolation given by $GM_B/Rc^2=0.1461$.

To convert these models, which are stored in the coefficient basis, into spatially defined particle-based quantities, we first lay down a grid of SPH particles in a hexagonal close-packed (HCP) lattice with constant lattice spacing and particle smoothing length. This grid is then treated as if we reflected around the $z=0$ plane, to take advantage of the vertical symmetry inherent in the problem. Each particle is treated as if it were really two particles for all SPH summations, one located above the $z=0$ plane, the other an equal distance below, both with half the true mass of the "real" particle. Since the vertical symmetry is enforced on a particle-based level, we solve all our field equations only for vertical angles $0<\theta<\pi/2$, and reflect the solutions for all points below the plane. The mass of each particle is initially set to be proportional to the density at the particle's position according to the quasiequilibrium model.

Next, using an iterative process, we calculate the SPH expression for the density of each particle, using Eq. (8), and adjust each particle's mass so that the SPH density matches the proper value from the initial model, stopping once the maximum difference for any particle is less than 0.25% of the star's central density. Particle velocities are assigned to match the quasiequilibrium model's velocity field, as are all other thermodynamic variables. Finally, we advance the velocities by half a time-step, using the same methods as in a standard iteration loop (see below), since we use a second-order accurate leapfrog algorithm (described in detail in [58]).

During each iteration, the first step is always the calculation of each particle's neighbor list, and the associated SPH forms for the density and other hydrodynamic terms. Once this is done, we perform a Euclidean transformation on our coordinates into a new frame (denoted by primed quantities), whose origin is defined to be the system center-of-mass, with the center-of-mass of each star lying on the x axis, making sure to transform the positions, velocities, and accelerations for each particle. In terms of the inertial frame coordinates of the NS centers-of-mass, $\vec{x}_1$ and $\vec{x}_2$, the transformation is given by

$$\phi' \equiv \tan^{-1}\frac{y_2-y_1}{x_2-x_1}, \tag{25}$$

$$x_{CoM}\equiv\frac{x_1+x_2}{2};\quad y_{CoM}\equiv\frac{y_1+y_2}{2}, \tag{26}$$

$$x'(x,y)\equiv(x-x_{CoM})\cos\phi'+(y-y_{CoM})\sin\phi', \tag{27}$$

$$y'(x,y)\equiv(y-y_{CoM})\cos\phi'-(x-x_{CoM})\sin\phi', \tag{28}$$

---

[2] http://www.lorene.obspm.fr/data/

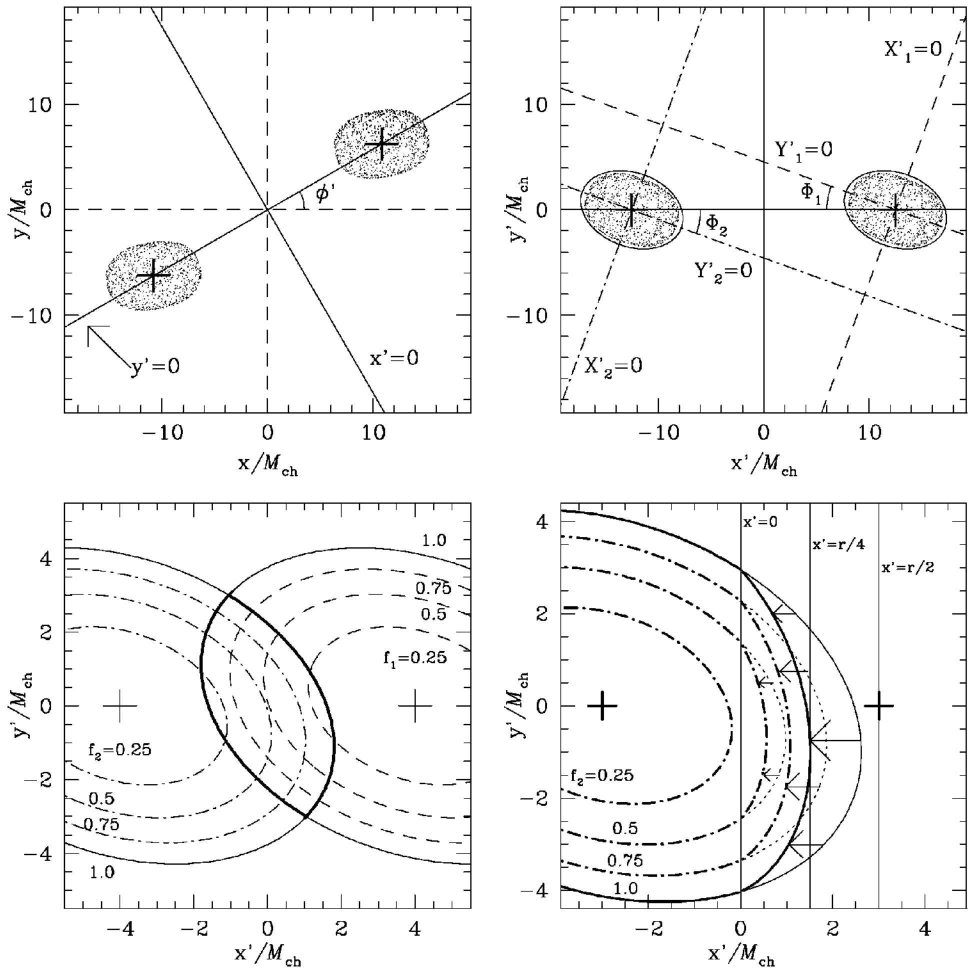

FIG. 2. A pictorial demonstration of the coordinate transformations described in Secs. III A and III B; the particle configuration is for demonstration purposes only, and was not taken from our calculations. In the upper left panel, we show a NS-NS binary in the $x-y$ (inertial) frame, as well as the $x'-y'$ frame, defined so that the centers-of-mass of the stars (crosses) lie equidistant from the origin on the x' axis [see Eqs. (25)–(29)]. In the upper right, we see the same system in the $x'-y'$ frame. The angles Φ_1 and Φ_2 are determined from the respective moment of inertia tensors using Eq. (30). The best fit ellipsoidal configurations, determined from Eqs. (31)–(38) are shown around each star, aligning with the $X'_q-Y'_q$ axes, determined from Eqs. (59) and (60). In the bottom left, we show isocontours for the radial functions f_1 and f_2, defined by Eq. (58), as well as the boundary of the overlap region (heavy solid line). Finally, in the bottom right, we show the rescaling of the surface function for very close configurations, showing only star 2 for clarity. Here, the binary separation is $r/\mathcal{M}_{ch}=6.0$, implying the maximum extent of the surface of star 2 is to $x'/\mathcal{M}_{ch}=r/4\mathcal{M}_{ch}=1.5$. We linearly rescale the surface function, as well as the corresponding values of f_2, for all points with $x'>0$.

$$\vec{x}'_{1,2}=\left(\pm\frac{R}{2},0,0\right);\quad R\equiv\sqrt{(x_2-x_1)^2+(y_2-y_1)^2}. \tag{29}$$

This transformation is shown in the upper left panel of Fig. 2. The next computational task is defining the shape of the innermost computational domains, calculated for sets of rays equally spaced in θ and ϕ, as measured from the center-of-mass of each star. We denote these surface functions $r(\theta_q,\phi_q)$, where the "q" subscript, taking the value 1 or 2, refers to angles measured in the primed frame of Eqs. (25)–(29) outward from the center-of-mass of star q. These surfaces are used to determine the position of the collocation points, which in turn are used as the basis for the entire spectral decomposition. While it is easy to find the point along any ray where the SPH density drops to zero, $r_{SPH}(\theta_q,\phi_q)$, we have found that such a set of points leads to unacceptable results from the field solver, especially with regard to the convexity of the matter distribution. If we ignore the density contributions of all particles whose density falls below some fixed value, say $\rho_{min}=0.0001$, the resulting surface function $\tilde{r}_{SPH}(\theta_q,\phi_q)$ is typically much more regular, but still is not an ideal choice, since we still cannot guarantee convexity. It should be noted that the field solver is entirely capable of handling matter sources which lie outside the innermost domain, although it does work best in the case where the surface of the matter matches the domain boundaries closely. For this reason, we restrict the shapes of the innermost domains to triaxial ellipsoidal configurations, oriented along the principal axes of the moment of inertia tensor for each star. The growing misalignment between the stars and the (rotated) coordinate system is a well-known effect, reflecting the tidal lag that develops in close binaries as matter tries to reconfigure itself in response to the rapidly changing gravitational field [68]. Thus, for each star, we calculate the angle Φ_q such that

$$\Phi_q = \frac{1}{2}\tan^{-1}\left(\frac{2I_{xy}}{I_{xx}-I_{yy}}\right), \tag{30}$$

where $I_{ij} \equiv \Sigma_a m_a (x'_a - x'_q)_i (x'_a - x'_q)_j$, and define our surface function $r(\theta_q, \phi_q)$ such that

$$r(\theta_q, \phi_q) = \left[\frac{\hat{x}^2}{a^2} + \frac{\hat{y}^2}{b^2} + \frac{\hat{z}^2}{c^2}\right]^{-1/2}, \tag{31}$$

where

$$\begin{aligned}\hat{x}(\theta_q, \phi_q) &\equiv \sin\theta_q(\cos\Phi_q \cos\phi_q + \sin\Phi_q \sin\phi_q)\\ &= \sin\theta_q \cos(\phi_q - \Phi_q),\end{aligned} \tag{32}$$

$$\begin{aligned}\hat{y}(\theta_q, \phi_q) &\equiv \sin\theta_q(\cos\Phi_q \sin\phi_q - \sin\Phi_q \cos\phi_q)\\ &= \sin\theta_q \sin(\phi_q - \Phi_q),\end{aligned} \tag{33}$$

$$\hat{z}(\theta_q, \phi_q) \equiv \cos\theta_q, \tag{34}$$

and a, b, and c are the axis lengths of the ellipse.

We have found it best to fix the axis ratios of the ellipse by computing the maximum extent of the surface defined by $\tilde{r}(\theta_q, \phi_q)$ in each principal direction, such that

$$a_0 = \max|\tilde{r}_{SPH}(\theta_q, \phi_q) \cdot \hat{x}(\theta_q, \phi_q)|, \tag{35}$$

$$b_0 = \max|\tilde{r}_{SPH}(\theta_q, \phi_q) \cdot \hat{y}(\theta_q, \phi_q)|, \tag{36}$$

$$c_0 = \max|\tilde{r}_{SPH}(\theta_q, \phi_q) \cdot \hat{z}(\theta_q, \phi_q)|. \tag{37}$$

Since this prescription can lead to some particles with $\rho_a > \rho_{min}$ falling outside of the surface, we multiply the distance in all directions by the smallest factor F_0 required to encompass all SPH particles whose density is greater than ρ_{min}, typically leading to an increase in linear size of no more than 2%, such that $a = a_0 F_0$, $b = b_0 F_0$, $c = c_0 F_0$, and

$$F_0 = \max\left[\tilde{r}(\theta_q, \phi_q)\sqrt{\frac{\hat{x}^2}{a_0^2} + \frac{\hat{y}^2}{b_0^2} + \frac{\hat{z}^2}{c_0^2}}\right]. \tag{38}$$

A typical surface fit is shown in the upper right panel of Fig. 2. The outer two domains are defined in terms of these new coordinate systems as well, to allow us to match field values and their derivatives at the boundaries.

Using the collocation points derived from these surfaces, our next task is to calculate the value of the field equation source terms at these points. Since calculating E and S for each SPH particle from Eqs. (16) and (17) would require a great deal of ultimately needless algebraic work, we do not calculate the SPH expressions for these quantities at collocation points. Instead, at every collocation point, we calculate the SPH expression for the rest mass density, the "rest pressure" $P_* \equiv k\rho_*^\Gamma$, and the density-weighted average velocity $\tilde{u}_i$. Using these values, as well as the field values from the previous iteration, we calculate γ_n from Eq. (12), and then E and S at every collocation point, and proceed to solve the field equations, using the iterative techniques described in GGTMB. Typically, we require ≈ 50 iteration loops to achieve a solution for which no field value varies by more than 1 part in 10^9 from one iteration to the next.

Once we have solved the field equations, we use the spectral expansion of the fields to calculate as much as we can of the terms in the force equation, before reading off the values at every particle position, which takes a significant amount of time. In practice, we use the spectral decomposition to calculate the prefactor for the pressure force term, NA^3, the vector sum of the terms involving derivatives of the conformal factor and lapse function, the nine first derivatives of the shift vector, and the radiation reaction terms. While it would be faster to calculate the force term involving the derivative of the shift vector completely in the spectral basis, we have found it to be inadvisable. This term alone is linear in the velocity, and it is inconsistent to use an averaged velocity in this term on the RHS of the force equation to calculate the rate of change of each particle's individual velocity on the LHS. Thus, denoting terms calculated within the spectral basis and exported to particle positions by "sb," and those calculated using SPH techniques only by "SPH," Eq. (9) is truly evaluated as

$$\begin{aligned}\frac{d\tilde{u}_i}{dt} = {} & [-NA^3]_{sb}\left[\frac{\nabla_i P}{\rho_*}\right]_{SPH} + \left[\frac{Nh(\gamma_n^2-1)}{A\gamma_n}\nabla_i A - h\gamma_n \nabla_i N\right]_{sb}\\ & - [\nabla_i N^j]_{sb}[\tilde{u}_j]_{SPH}.\end{aligned} \tag{39}$$

After calculating the forces on each particle and advancing the velocities by a full time step, we are still left with the task of recomputing Eq. (7), which relates v^i and $\tilde{u}_i$. Since the sources for the field equations are velocity dependent, and we have just advanced $\tilde{u}$, we rerun the field solver with the new values of $\tilde{u}_i$, and compute Eq. (7) in the form

$$v^i = [N^i]_{sb} + \left[\frac{1}{A^2 h u^0}\right]_{sb}[\tilde{u}_i]_{SPH}. \tag{40}$$

Finally, we record the GW strains, ADM mass and system angular momentum, after rotating all positions, velocities, and accelerations back to the inertial frame by means of the inverse Euclidean transformation to the one at the beginning of the iteration.

There are several different ways to calculate the ADM mass numerically, all of which should be equivalent to Eq. (21), yielding an important check on the code. First, we calculate the system's ADM mass using by taking a surface integral at spatial infinity [see Eq. (65) of GGTMB],

$$M_0 = -\frac{1}{2\pi}\oint_\infty \partial^i A^{1/2} dS_i. \tag{41}$$

This quantity can be compared to the particle-based expression, with two important caveats. Since the extrinsic curvature contribution to the ADM mass, Eq. (23), does not have compact support, there is no way to convert the integral into a sum over particles that have a different spatial extent. Second, noting our concerns about exporting large numbers of terms from the spectral representation to particle positions, we perform some of the algebra involved in determining the ADM mass in the spectral representation. In the end, the particle-based expression for the ADM mass becomes

$$M_0 = \left(\int \rho_2 d^3x \right)_{sb} + \sum_a m_a \left[\frac{\rho_1}{\rho_*} \right]_{sb}, \tag{42}$$

and we define $\tilde{\rho} \equiv \rho_1/\rho_*$ as the ratio of ADM mass density to rest mass density, calculated using LORENE techniques at all SPH particle positions.

In a similar fashion, there are two ways to calculate the system angular momentum. We check the behavior of J in the spectral basis [see Eq. (67) of GGTMB],

$$J_i = \frac{1}{16\pi} \epsilon_{ijk} \oint_\infty (x^j K^{kl} - x^k K^{jl}) dS_l, \tag{43}$$

as well as the SPH expression for the angular momentum,

$$J_i = \epsilon_{ijk} \sum_a m_a x^j \tilde{u}_k. \tag{44}$$

Since the CF formalism is time-symmetric, the dissipative effects of gravitational radiation back reaction have to be added in by hand, just as they are for PN calculations. Previous PN calculations of binary NS systems (FR and [39]) have typically employed the exact 2.5PN formulas introduced by [40] to describe lowest-order GW losses from the system. Unfortunately, those equations are not applicable to CF calculations, since they are written in terms of fields defined in the PN approximation that differ from those defined in the CF approximation. For this work, we follow the approach of [45], using the slow-motion approximation to estimate the radiation reaction potential of the system. While this method contains some obvious flaws, most obviously the fixed spatial dependence of the radiation reaction potential, it does yield a back reaction force which is quantitatively correct in overall magnitude. These approximations should not affect our calculations to a large degree. While the infall velocity of the binary prior to plunge is driven by the GW back reaction, a different regime occurs after dynamical instability sets in. During this period, the evolution is almost completely hydrodynamic in nature [58]. While the chosen GW back reaction treatment may affect the final mass and angular momentum of the resulting merger remnant, it will play only a secondary role in the detailed evolution of the fluid configuration, since GW back reaction becomes less important during the coalescence.

From Eq. (51) of [45], the radiation reaction force in the slow-motion approximation is given by adding a term,

$$a_{i:reac} = N^2 h u^0 \nabla_i \chi, \tag{45}$$

to the RHS of Eq. (9). We define the radiation reaction potential χ in a similar but slightly different way than their Eq. (56), such that

$$\chi = \frac{1}{5} x^k x^l Q_{kl}^{[5]}, \tag{46}$$

similar to the approach taken in [48]. As they do, we define the quadrupole moment as

$$Q_{kl} = STF\left[\int \rho_{ADM} x_k x_l d^3x \right], \tag{47}$$

noting that our "ρ_{ADM}" corresponds to many other authors' S_ψ, or some multiple thereof. The expression "STF" refers to the symmetric, trace-free component of the tensor, which is linked to the gravitational radiation production in the quadrupole limit. As noted previously in our calculations of the system's ADM mass, we can evaluate the contribution from ρ_1 using standard SPH summation techniques, but the second term can only be found using LORENE integration techniques. Thus,

$$Q_{kl} \equiv Q_1 + Q_2 = \mathrm{STF}\left[\left(\sum_a m_a \bar{\rho}_a x_a^k x_a^l \right) + \left(\int d^3x \rho_2 x^k x^l \right)_{sb} \right], \tag{48}$$

where Q_1 and Q_2 reflect the contributions from ρ_1 and ρ_2, respectively. Using SPH, we can take the first time derivative of the former half, so long as we ignore the Lagrangian derivative $d\rho_1/dt$, which should be essentially negligible during our calculations. We find

$$(\dot{Q}_1)_{kl} = STF\left[\int \rho_1 (x_k v_l + x_l v_k) d^3x \right]. \tag{49}$$

To calculate the rate of change of the extrinsic curvature, we assume that the time variation in the tensor is due solely to the orbital motion (rather than an overall change in magnitude of the tensor components in a corotating frame), which yields

$$(\dot{Q}_2)_{xx} = -(\dot{Q}_2)_{yy} \approx 2\omega (Q_2)_{xy}, \tag{50}$$

$$(\dot{Q}_2)_{xy} \approx 2\omega \left[\frac{(Q_2)_{xx} - (Q_2)_{yy}}{2} \right], \tag{51}$$

where the factor 2ω reflects the fact that the quadrupole tensor makes two cycles during every orbital period. To calculate the fifth time derivative of the quadrupole tensor, we use the same technique with both components of the tensor, finding

$$Q_{kl}^{[5]} \approx 16\omega^4 \dot{Q}_{kl}, \tag{52}$$

where in all cases the system's instantaneous angular velocity is calculated as the ratio of the angular momentum to the moment of inertia,

$$\omega \equiv \frac{\sum_a m_a(x_a(v_y)_a - y_a(v_x)_a)}{\sum_a m_a(x_a^2+y_a^2)}, \tag{53}$$

which holds exactly in the quadrupole limit for synchronized binaries.

Calculating the GW signal and energy spectrum is a more straightforward task which can be done after the calculation is finished. We calculate the GW strain in two independent polarizations for an observer located at a distance d from the system perpendicular to the orbital plane from the lowest-order quadrupole expressions,

$$dh_+ = Q_{xx}^{[2]} - Q_{yy}^{[2]}, \tag{54}$$

$$dh_\times = 2Q_{xy}^{[2]}, \tag{55}$$

where we calculate the second time derivatives of the quadrupole tensor by numerically differentiating the results from Eq. (49). In terms of the Fourier transform of the quadrupole moment,

$$\tilde{Q}_{kl}^{[2]}(f_{GW}) \equiv \int e^{2\pi i f t} Q_{kl}^{[2]}(t)\,dt, \tag{56}$$

where $f_{GW} \equiv 2 f_{orb}$ is the *GW* frequency, the GW energy spectrum is computed as [63]

$$\frac{dE}{df_{GW}} = \pi f_{GW}^2 \left(\frac{8}{15}[(\tilde{Q}_{xx}^{[2]} - \tilde{Q}_{yy}^{[2]})^2 + (\tilde{Q}_{xx}^{[2]} - \tilde{Q}_{zz}^{[2]})^2 + (\tilde{Q}_{yy}^{[2]} - \tilde{Q}_{zz}^{[2]})^2] + \frac{8}{3}[(\tilde{Q}_{xy}^{[2]})^2 + (\tilde{Q}_{xz}^{[2]})^2 + (\tilde{Q}_{yz}^{[2]})^2] \right). \tag{57}$$

B. Merging systems

As the stars in the binary system spiral inward, they reach a point where the density distributions begin to overlap as matter from the inner edge of each star falls onto the surface of the other. Our field solver can handle this situation, since it does not assume that the matter sources are spatially distinct, but the surfaces required to envelop the particles from each star would become poorer and poorer fits to the two NS. Noting this, we alter the approach described above in a number of ways when the particles first cross through the inner Lagrangian point at the center of the system, in such a way that the surfaces we define for each star always remain smooth and still do an acceptable job of describing the true density distribution in a meaningful way.

Once the binary separation shrinks sufficiently, matter streams from the inner edge of each NS toward the other NS, flowing along the surface of the companion. These counter-streaming, low-density flows lead to the formation of a vortex sheet (FR3). Mass transfer typically occurs before the triaxial ellipsoidal surfaces used to define the two stars overlap, since particles crossing from one star to another generally fall beneath the density cut used to define each surface. To account properly for the star to which each particle is bound, we declare particle "a" a member of the first star if $x'_a < 0$ and a member of the second star if $x'_a > 0$, at least for the purposes of defining each star's center of mass and tidal lag angle, as described in Eqs. (25)–(38).

This approach entails further alterations once the ellipsoidal computational domains from each star begin to overlap. Using the y'-axis as the dividing line between the two stars is fine for determining the center-of-mass, tidal lag angle, and ellipsoidal surface for each star, but it is inappropriate to draw a fixed line at $x'=0$ when calculating field equation source terms. These would induce a sudden density drop from finite density at small negative values of x' to zero density at positive x' values (for the first star, vice versa for the second), leading to large Gibbs effects. It is equally inappropriate to count one particle as a member of both stars, since we would end up double-counting its density contribution to the field equations. Instead, we introduce a weight function $f_a \equiv f(\vec{x}'_a)$, for each particle in the overlapping region in such a way that $f=0$ at the surface of star 1, $f=1$ on the surface of star 2, and $0<f<1$ in a spatially differentiable way within the overlap region. To do so, we define f_1 and f_2, the fractional squared distance outward a point lies from the center of each star to the surface. For the first star,

$$f_q(x') \equiv \frac{(X'_q)^2}{a^2} + \frac{(Y'_q)^2}{b^2} + \frac{(z')^2}{c^2}, \tag{58}$$

where

$$X'_q \equiv x_q \cos\Phi_q + y' \sin\Phi_q, \tag{59}$$

$$Y'_q \equiv -x_q \sin\Phi_q + y' \cos\Phi_q, \tag{60}$$

are the rotated coordinates used to define the (tidally lagging) ellipsoidal surface of the star, and $x_q(x') \equiv x' - x'_q$ is the distance in the x'-direction from the center-of-mass of star q. A picture of these quantities is shown in the bottom left panel of Fig. 2. In terms of f_q, we define our overlap function f_a for each particle such that

$$f_a = f(\vec{x}'_a) = \frac{(1-f_1)^3}{(1-f_1)^3 + (1-f_2)^3}. \tag{61}$$

For the first star, source terms in the field equations are evaluated as

$$(\rho_*)_1 = \sum_a m_a f_a W_a, \tag{62}$$

$$(P_*)_1 = \frac{(\rho_*)_1}{(\rho_*)_1 + (\rho_*)_2} k[(\rho_*)_1 + (\rho_*)_2]^\Gamma, \tag{63}$$

$$(\tilde{u}_i)_1 = \frac{\sum_a m_a f_a (\tilde{u}_i)_a W_a}{\sum_a m_a f_a W_a}, \tag{64}$$

TABLE II. A summary of the runs presented in this paper.

Run	Description	See Sec. no.
OV1	Equilibrium OV model, $GM_0/Rc^2=0.126$	IV A
OV2	Nonequilibrium OV model, $R_0=1.1R_{eq}$	IV A
OV3	Same as OV2, w/relaxation drag	IV A
DC5	Collapsing dust cloud, $M_0=1$, $R_0=5$	IV B
DC10	Collapsing dust cloud, $M_0=1$, $R_0=10$	IV B
DC50	Collapsing dust cloud, $M_0=1$, $R_0=50$	IV B
QC1	Quasicircular binary orbit w/o rad. reac., $r_0/\mathcal{M}_{ch}=19.91$	IV C
QC2	Quasicircular binary orbit w/o rad. reac., $r_0/\mathcal{M}_{ch}=20.42$	IV C
QC3	Quasicircular binary orbit w/o rad. reac., $r_0/\mathcal{M}_{ch}=22.98$	IV C
RR1	Full binary evolution w/rad. reac., $r_0/\mathcal{M}_{ch}=19.91$	V B
RR2	Full binary evolution w/rad. reac., $r_0/\mathcal{M}_{ch}=22.98$	V A

where W_a is the smoothing kernel function evaluated between the collocation point and overlapping particles. Complementary expressions hold for the second star by substituting $(1-f_a)$ for f_a.

This approach allows us to calculate the fields properly using spectral methods well into the merger, but a final modification is necessary to bring us to the point where the density profile of the matter can better be described by viewing it as a single object. When the inner edge of one star overlaps the center of the other star, the density profile typically becomes bimodal, leading to spurious results from the spectral expansion. To guard against this happening, we use a relatively simple approach. If the surface of one ellipse extends more than halfway from $x'=0$ toward the center-of-mass of the other star at $x'_q=\pm R/2$, we linearly rescale all surface points that lie across the y'-axis. Thus, defining $x_q(\theta_q,\phi_q)=r(\theta_q,\phi_q)\sin\theta_q\cos\phi_q$ in accordance with our previous notation, if the surface of either star extends to a maximum value $x_{q:max}\equiv\max(|x_q|)>3R/4$ [or in other words, if $\max(|r(\theta_q,\phi_q)\sin\theta_q\cos\phi_q-x'_q|)>R/4$], we adjust all points on the other side of the y'-axis, yielding

$$x_{q:new}(\theta_q,\phi_q)=\frac{R}{2}+\frac{R}{4}\left(\frac{x_{q:old}(\theta_q,\phi_q)-R/2}{x_{q:max}(\theta_q,\phi_q)-R/2}\right)\quad\text{for all points with } x_q(\theta_q,\phi_q)>R/2. \tag{65}$$

To evaluate the weight function, we adapt the x'-dependence correspondingly, such that for particles with $x_q>R/2$

$$f_{a:new}(\vec{x}_q)=f_{a:old}(\kappa\cdot\vec{x}_q), \tag{66}$$

where the rescaling factor $\kappa\equiv R/2+(x_q-R/2)[(x_{q:max}-R/2)/(R/4)]$. The bottom right panel of Fig. 2 demonstrates this last coordinate transformation.

Eventually, the system will reach a point where it can no longer be properly described as a binary, and our field solver fails to converge. Before this happens, we reach a point where we can describe the system as a rapidly rotating single star, using all the methods described above for computing the evolution, but now assuming that all particles comprise the same star. We have found that our results are independent of the exact moment at which we make this conversion. In the following discussion, we will show the results for runs where we perform the conversion at the earliest possible time for which the field solver will converge to a solution when the matter configuration is treated as a single star.

IV. TEST CALCULATIONS

We have performed several tests to check the accuracy and numerical stability of our code, for both single-star and binary systems. We have studied the behavior of the code for spherically symmetric problems for which the exact field solution can be calculated semi-analytically: the Oppenheimer-Volkov solution for a static spherical star and the collapse of a pressureless dust cloud initially at rest. We have also calculated the dynamical evolution of the binary quasiequilibrium models calculated in TG, without the inclusion of radiation reaction forces. A summary of all our calculations, including those used for testing the code, can be found in Table II.

A. The Oppenheimer-Volkov (OV) test

Since the CF formalism is exact for spherically symmetric systems, which can always be described in isotropic coordinates, it is fair to expect that any working code should be able to reproduce the well-known Oppenheimer-Volkov solution exactly, noting that the traditional form of the OV solution needs to be rewritten into CF coordinates. With $\rho'\equiv\rho(1+\epsilon)$ as the total energy density (including both the rest and internal energy densities), the OV equations are typically written

$$\frac{dm}{d\bar{r}}=4\pi\bar{r}^2\rho', \tag{67}$$

$$\frac{dP}{d\bar{r}} = -\frac{(\rho' + P)(m + 4\pi P \bar{r}^3)}{\bar{r}^2 - 2m\bar{r}}, \tag{68}$$

$$\frac{d\Phi}{d\bar{r}} = \frac{(m + 4\pi P \bar{r}^3)}{\bar{r}^2 - 2m\bar{r}}, \tag{69}$$

for an interior metric in the form

$$ds^2 = -e^{2\Phi}dt^2 + \left(1 - \frac{2m}{\bar{r}}\right)^{-1} d\bar{r}^2 + \bar{r}^2 d\Omega^2, \tag{70}$$

and exterior metric in the Schwarzchild form

$$ds^2 = \left(1 - \frac{2M_0}{\bar{r}}\right)dt^2 + \left(1 - \frac{2M_0}{\bar{r}}\right)^{-1} d\bar{r}^2 + \bar{r}^2 d\Omega^2, \tag{71}$$

where the star's total gravitational (ADM) mass $M_0 \equiv m(\bar{r}_s)$, and $\bar{r}_s$ is the Schwarzchild coordinate radius of the stellar surface. A quick comparison with the CF metric, Eq. (2), shows that $N = e^{\Phi}$ inside the star, but the conversion between A and Φ requires more care, since we have to determine the relationship between the two coordinate radii $r(\bar{r})$. The simplest way to determine the change of coordinates is to solve for the values of r_s and $\bar{r}_s$, the radii of the stellar surface, using the asymptotic behavior of the exterior solution (following the same logic used in exercise 31.7 of [64]). Comparing the radial and angular parts of the metric, we find

$$A^2 dr^2 = \left(1 - \frac{2M_0}{\bar{r}}\right)^{-1} d\bar{r}^2, \tag{72}$$

$$A^2 r^2 = \bar{r}^2. \tag{73}$$

Dividing and taking a square root, we find

$$\frac{dr}{r} = \frac{d\bar{r}}{\sqrt{\bar{r}(\bar{r} - 2M_0)}}. \tag{74}$$

Integrating yields

$$\ln r + k = 2\ln(\sqrt{\bar{r}} + \sqrt{\bar{r} - 2M_0}), \tag{75}$$

and we find

$$kr = (\sqrt{\bar{r}} + \sqrt{\bar{r} - 2M_0})^2 = 2\bar{r} - 2M_0 + 2\sqrt{\bar{r}(\bar{r} - 2M_0)}. \tag{76}$$

The asymptotic behavior at infinity indicates that we must have $k = 4$, so our final expression for $r(\bar{r})$ takes the form

$$r = \frac{1}{2}(\bar{r} - M_0 + \sqrt{\bar{r}(\bar{r} - 2M_0)}). \tag{77}$$

For a star with Schwarzchild surface radius $\bar{r}_s$, we find that the CF surface radius is given by

$$r_s = \frac{1}{2}(\bar{r}_s - M_0 + \sqrt{\bar{r}_s(\bar{r}_s - 2M_0)}), \tag{78}$$

the surface value for the conformal factor is

$$A_s = \frac{\bar{r}}{r} = \frac{2\bar{r}_s}{\bar{r}_s - M_0 + \sqrt{\bar{r}(\bar{r} - 2M_0)}}, \tag{79}$$

and the lapse function at the surface is given by

$$N_s = \sqrt{1 - \frac{2M_0}{\bar{r}_s}}. \tag{80}$$

To solve for the interior metric, we add an equation to the OV set to take into account the different radial schemes, defining a scale free conformal radius satisfying a boundary condition $\lim_{\bar{r}\to 0} r_0 = \bar{r}$ whose radial behavior is given by

$$\frac{dr_0}{d\bar{r}} = \frac{r_0}{\sqrt{\bar{r}(\bar{r} - 2m)}}. \tag{81}$$

This yields an expression for $r_0(\bar{r})$ which is defined up to an arbitrary multiplicative constant k, such that $r_0 = k \cdot f(\bar{r})$, where f is determined from the mass distribution. To find $r(\bar{r})$, we merely set $k = r_s/(r_0)_s$, which implies $r = \bar{r} r_s/(r_0)_s$ and determine A from Eq. (73).

To test the code, we ran three calculations whose results could be compared with well-known semi-analytic solutions. First, we constructed an equilibrium model for an isolated NS, whose density profile was given by an OV solution for a $\Gamma = 2$ EOS, with unit ADM mass, and a conformal radius $r_s = 6.874$. The solution has a total baryonic mass $M_b = 1.066$, and an areal radius $\bar{r}_s = 7.913$. We started run OV1 by taking this solution as an initial condition, and used it to test the overall stability of the code for equilibrium configurations. Next, we constructed a similar model with the same mass and EOS, but scaled to an initial radius 10% larger. Run OV2 is a dynamical calculation started from this initial condition using our standard evolution code, enabling us to study the oscillations around our equilibrium solution. Last, we took the nonequilibrium configuration from run OV2, but added a "relaxation" drag term of the form $-\tilde{u}_i/t_{relax}$ to the RHS of the force equation, Eq. (9), with $t_{relax}/M_0 = 7.9$. This provides an overdamped force for run OV3 since the dynamical time scale $t_D/M_0 \equiv (G\rho)^{-0.5} = 18$. All three runs were followed until $t/M_0 = 120$, corresponding to 6.7 dynamical times for the NS, and in all cases radiation reaction was turned off.

In Fig. 3, we show the radial profiles of the lapse function and conformal factor at $t/M_0 = 100$ for runs A and C, along with the correct OV solution. It is no surprise that run A has essentially remained the same, since the initial field values were essentially exact, but it is reassuring that run C has converged as well toward the same solution. Indeed, results for configurations at later times continue to converge toward the exact solution. In Fig. 4, we show the evolution of the

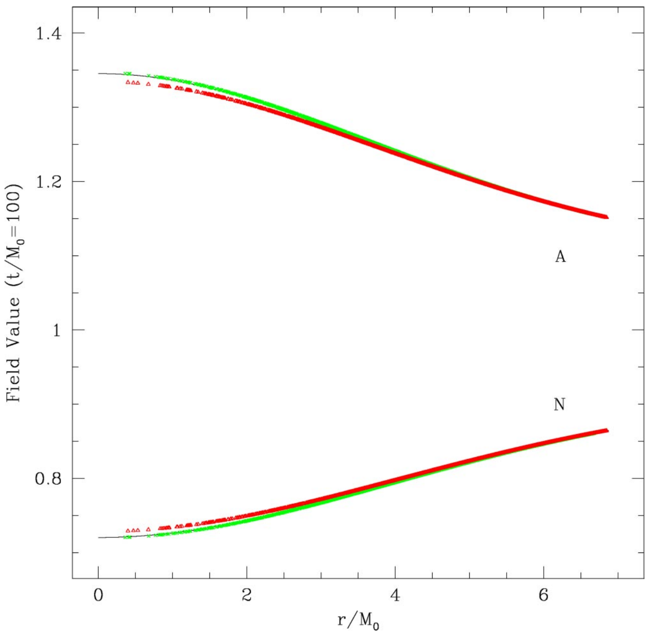

FIG. 3. Conformal factor A and lapse function N for an Oppenheimer-Volkov solution with a $\Gamma=2$ polytropic EOS, and conformal radius $r_s/M_0=6.874$ (solid lines), compared to our computed values at $t/M_0=100$ for two models: run OV1 started from equilibrium (crosses) and run OV3 started from a configuration 10% larger with a velocity damping term used to drive the system toward equilibrium (triangles). The agreement is within 1% for all particles. Units are defined such that $G=c=1$. All masses, lengths, and times in the OV and dust cloud calculations are made dimensionless by scaling results against the system's initial gravitational (ADM) mass. Note that the conformal radius is not equivalent to the areal radius typically used in solving the OV equation.

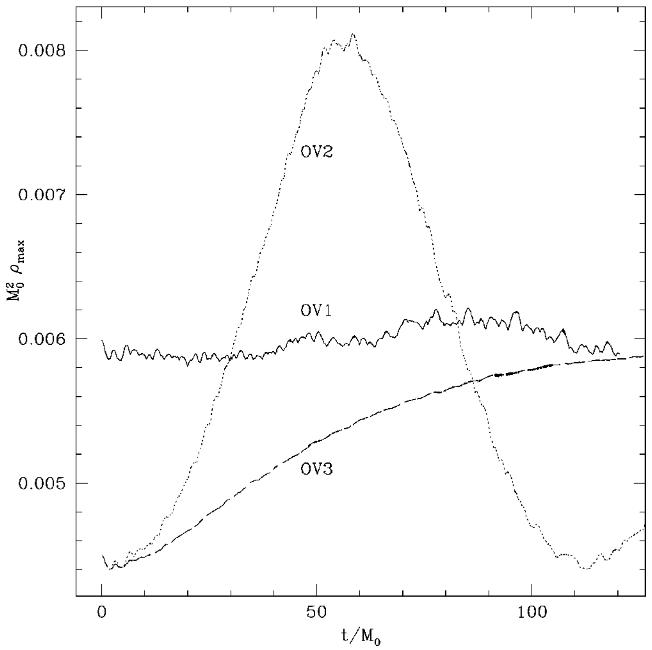

FIG. 4. Evolution of the maximum density for three runs based on the OV solution described in Fig. 3. Run OV1 (solid line) was started from equilibrium, and shows only small variations which result from typical uncertainties in SPH summation. Run OV2 (dotted line) used the same EOS, but was started from a radius 10% smaller than the equilibrium value, showing sinusoidal oscillations with a period of $T/M_0=112$ and no systematic drift. Run OV3 (dashed line) was started from the same configuration as run B, but with an overdamped drag term to force the system toward equilibrium, converging rapidly toward the proper value of $M_0^2\rho_{max}=0.006$.

maximum central density for the three runs, as well as the predicted value from the OV solution. The maximum density from run A stays near this value throughout the evolution, with small deviations which result from the unavoidable discretization effects present in SPH; in general, SPH will yield very accurate global integrals over a mass distribution, since numerical noise smoothes out, but demonstrates significant noise in quantities defined for individual particles, which vary iteration to iteration as each particle's neighbor list adapts to current conditions. The maximum density for run B oscillates around the proper value with a period of $T/M_0=112$, showing no signs of systematic drift. This is very close to the proper value for the limiting case of infinitesimal radial variations, $T/M_0=104$, which we find by interpolating from the values given in Table A18 of [65], after scaling their results to our units.

B. Spherical dust cloud collapse

To further test the dynamical aspects of the code, we computed the evolution of a uniform density dust cloud, i.e., a spherical distribution of matter with zero pressure, started initially from rest. This is a familiar problem from cosmology, and the solution is well known, but the conversion to CF coordinates and the matching conditions at the surface of the dust cloud make the resulting expressions considerably more complicated. The complete description of the metric as a function of time was derived for the case of both maximal time-slicing [66] and polar time-slicing [67]; it is the former case which can be compared to our results. In this approach, the field values and CF time and position variable values are computed by solving a set of ordinary differential equations which describe the behavior of the fields in terms of the comoving time and space variables. Using these, it is a simple process of interpolation to derive the fields as functions of CF time and position. We checked our integration code by comparing our results against the plots in [66], finding perfect agreement.

To construct our initial configuration, we used essentially the same techniques described above. Particles were laid out in an HCP lattice, with masses set proportional to the analytically known value of $\rho_*(r)$, which we derive as follows. Note that ρ_* varies with radius; it is $\rho(r)$ that is initially uniform.

The total mass of the cloud was set to unity, and the initial radius in comoving coordinates to $\overline{r_s}$, the parameter used for all figures in [66]. The initial metric in comoving coordinates, for a cloud with unit mass and comoving radius $\overline{r_s}$, is given by

$$ds^2=-d\tau^2+a(\tau)^2(d\chi^2+\sin^2\chi d\Omega^2), \tag{82}$$

$$a(\tau=0)\equiv 2/(\sin\chi_s)^3, \tag{83}$$

$$\overline{r_s}\equiv 2/(\sin\chi_s)^2, \tag{84}$$

with the exterior metric described by the Schwarzchild form, Eq. (71), with $\overline{r}=a(\tau=0)\sin\chi$. In terms of χ_s, the CF radius is given by

$$\begin{aligned} r_s &= \frac{1}{2}\left(\overline{r_s}-M_0+\sqrt{\overline{r_s}(\overline{r_s}-2M_0)}\right) \\ &= \frac{1}{2}\left(\frac{2}{\sin^2\chi_s}-1+\sqrt{\frac{4}{\sin^4\chi_s}-\frac{4}{\sin^2\chi_s}}\right) \\ &= \frac{1}{2}\,\frac{1+\cos\chi_s}{1-\cos\chi_s}. \end{aligned} \tag{85}$$

Equating interior metric coefficients, we set $A dr = a d\chi$ and $Ar = a\sin\chi$, dividing and then integrating to find

$$r \propto \left(\frac{1-\cos\chi}{1+\cos\chi}\right)^{1/2}, \tag{86}$$

$$= \frac{1}{2}\left(\frac{1-\cos\chi}{1+\cos\chi}\right)^{1/2}\left(\frac{1+\cos\chi_s}{1-\cos\chi_s}\right)^{3/2}, \tag{87}$$

where the proportionality constant is determined from Eq. (85). The initial conformal factor can now be written down, since

$$A=\frac{a\sin\chi}{r}=\frac{4(1+\cos\chi)}{(1+\cos\chi_s)^3}, \tag{88}$$

and we can simplify the resulting expression by noting that $\cos\chi_s=(2r_s-1)/(2r_s+1)$ and $\cos\chi=(1-r^2/2r_s^3)/(1+r^2/2r_s^3)$. Since the matter starts from rest, we know that $u_i=0$ initially, and thus $\gamma_n=1$ everywhere, and we find the initial rest-mass density profile is given as a function of radius by

$$\rho_* = \gamma_n A^3\left(\frac{3M}{4\pi\overline{r_s^3}}\right)=\frac{3}{4\pi r^3}\left(\frac{1+\dfrac{1}{2r_s}}{1+\dfrac{r^2}{2r_s^3}}\right)^3. \tag{89}$$

Once the initial particle configuration was set, we calculated the dynamical evolution of the system using the same techniques described above for the OV case. Since the pressureless material had no outwardly directed force, the inevitable fate of the system was collapse to a BH.

To allow for direct comparison with the figures shown in [66], we computed the evolution of a dust cloud with unit ADM mass and an initial areal radius $\overline{r_s}=10$, just as they did. In Fig. 5, we show the evolution of a set of equally spaced Lagrangian tracer particles compared to the exact semianalytic solution we computed. This corresponds to their Figs. 8, 9, with two slight differences. Our figures are plotted in CF coordinates, rather than comoving coordinates, and our tracers are equally-spaced in radius, not in increments of enclosed mass. For comparison with their Fig. 9, we also show the more familiar areal radius of the cloud, which roughly satisfies the relation $r_s\approx\overline{r_s}-1$ initially. We see the agreement between our calculation and the exact solution is very good throughout the evolution, up until $t/M_0\approx 38$, where a slight discrepancy begins to develop, primarily at the surface of the cloud. This time corresponds closely with the formation of an event horizon for the system, shown as a dotted line, starting at the center at $t/M_0=38$ and moving outward, reaching the surface of the cloud at $t/M_0=43.4$, shown as a horizontal line. This late time discrepancy has two sources. The first is that SPH, which by definition produces a differentiable density field, cannot reproduce the step-function density drop at the surface of the dust cloud. This explains to a large degree why the outermost tracers diverge furthest from their exact path. In addition, the large field values and gradients found around the event horizon present a challenge for our field solver. We typically see a dramatic increase during this period in the number of relaxation iterations required to converge to a sufficiently accurate solution.

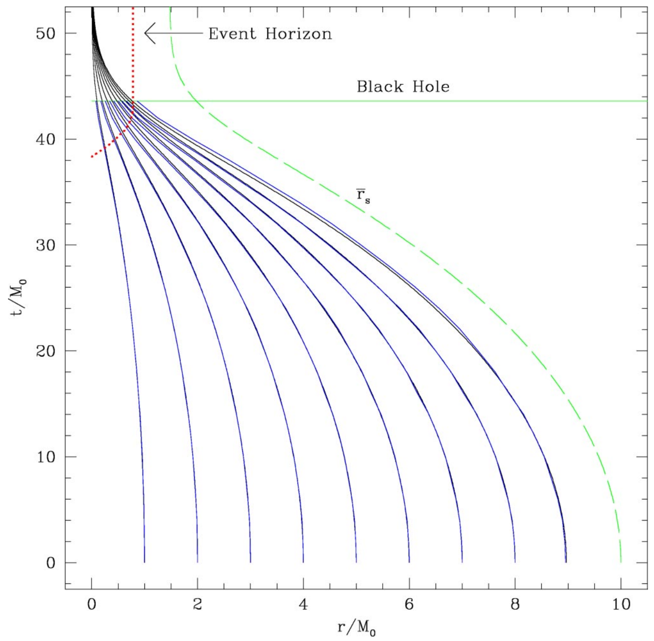

FIG. 5. A comparison between the actual paths traced out by a set of equally-spaced Lagrangian tracers in run DC10, our calculation of a collapsing dust cloud with unit ADM mass and initial areal radius $\overline{r_s}=10$, (dashed lines) and the exact semianalytical solution of [66], shown as solid lines. All radii are shown here in conformal coordinates. We see excellent agreement up until the point where an event horizon forms at the center of the cloud, at $t/M_0=38$. The event horizon moves outward (heavy dotted line), eventually enclosing the entire cloud at $t/M_0=43.4$, shown as a horizontal line in the figure. At this point, when the matter can be properly defined as a BH, our field solver stops converging. For comparison with Fig. 9 of [66], we also show, as a long-dashed line, the exact solution for the cloud's surface in comoving (areal) radii, $\overline{r_s}(t)$.

In Fig. 6, we show the evolution of the conformal factor A

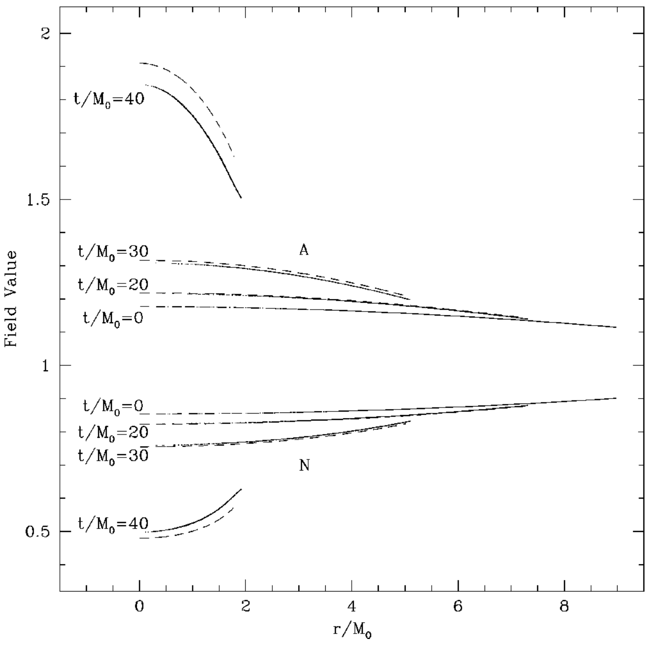

FIG. 6. The evolution of the conformal factor A and Lapse function N for the dust cloud in run DC10, compared to the exact solution. We see, at $t/M_0=0$, 20, 30, and 40, the SPH particle values for the lapse (the four curves with values less than 1.0) and conformal factor (values greater than 1.0), shown as points, and the exact solutions, shown as dashed lines. The agreement is good up until $t/M_0=30$, but at $t/M_0=40$ we see some quantitative disagreement, since the field solver breaks down as we near the point where the cloud collapses completely into a BH.

and lapse function N for the dust cloud, again in comparison to the exact solution, at times $t/M_0=0$, 20, 30, and 40. We see again that our code can reproduce the proper solution past $t/M_0=30$, but by $t/M_0=40$ shows nontrivial deviations from the proper solution. At $t/M_0=40$, the relative error in the metric fields and position of the Lagrange radii is approximately 4%, growing to roughly 15% by the time the event horizon encompasses the entire mass distribution. In all cases, the deviations from the correct solution take the same form: our computed field values are closer to unity (and the previous timestep's solution) than we would expect from the semianalytic solution.

This behavior was confirmed by testing the collapse of dust clouds with initial areal radii of $\overline{r_s}=5$ and $\overline{r_s}=50$. In both cases, we find extremely accurate results until the event horizon forms, at which point our accuracy degrades to a noticeable extent. The effect seems to depend primarily on the formation of an event horizon in the system, and not on the relative change of the density or various field quantities. We have concluded that the relaxation techniques used in the code have difficulty in their current form in handling the steep spatial gradients in the shift function near the event horizon (see Fig. 2 of [66]), and we are working on techniques to better handle this situation. Of particular importance is altering the relaxation parameters of the iterative scheme used by the field solver in the presence of these large field values and gradients near the event horizon, to correct for the systematic drift away from the expected values.

C. Circular orbits of quasiequilibrium configurations

Finally, to test out the overall stability of the code, we evolved several quasiequilibrium binary configurations using our code, but without adding in the radiation reaction drag terms. Since the CF formalism is time-symmetric, we expect that any stable quasiequilibrium model should yield a circular orbit, maintaining a constant binary separation, ADM mass, and internal rotation profile, among other parameters. Here, we chose models at an initial binary separation of $r_0/\mathcal{M}_{ch}=19.91$, 20.42, and 22.97 from the $M/R=0.14$, 0.14 equal-mass sequence of TG, denoting the resulting calculations as runs QC1, QC2, and QC3, respectively. For NS with ADM masses of $M_0=1.4\ M_\odot$, these separations correspond to 33.64, 34.51, and 38.81 km, respectively. The innermost of these represented the limiting case found for this sequence just before formation of a cusp at the inner edge of the two NS.

As a first check of our code, we compared the orbital frequency determined from our dynamical runs to the known value for each model taken from the quasiequilibrium sequence. We found excellent agreement between the orbital periods computed from our runs, $T/\mathcal{M}_{ch}=422.6$, 438.2, and 506.4, and those determined by TG, $T/\mathcal{M}_{ch}=422.8$, 438.0, and 519.7, for runs QC1, QC2, and QC3, respectively.

There are several conserved quantities which should be respected in the time-symmetric CF formalism, allowing for further code tests. In Fig. 7, we show the evolution of the binary separation for the runs. For each run, the orbital period is shown with tick marks. We see in each case that the orbit is stable, with variations in the binary separation of no more than 4% during the first two orbits. The time scale for the radial variations is similar to the orbital period, but not an exact match; this reflects both the effects of GR as well as the slight degree of time-asymmetry present in the numerical implementation of the CF formalism. We note that the deviations from circularity were largest for run QC3, which had the largest binary separation. We believe this results from the larger relative magnitude of the spurious initial velocities that result from deviations away from equilibrium in the initial condition; while these terms are of essentially constant magnitude in all three runs, the equilibrium velocity field has the smallest magnitude at the largest separation.

Run QC1 was started from the innermost point along this binary NS equilibrium sequence, and the binary performs three complete orbits with no sign of plunging behavior. As such, these results can be taken as the first direct proof that the entire equilibrium sequence is stable, and suggest that these configurations should be reasonably accurate approximations to the true physical state of merging binaries. Further evidence of this claim is presented below in Sec. V B, when we describe the results of our calculations with radiation reaction effects included. Note that this result is not unexpected given the absence of a turning point (minimum of ADM mass and total angular momentum) along this irrotational equilibrium sequence. Indeed, while such a turning point along an equilibrium sequence of *corotating* binaries marks the onset of *secular instability*, a true *dynamical instability* is usually associated with a turning point along an

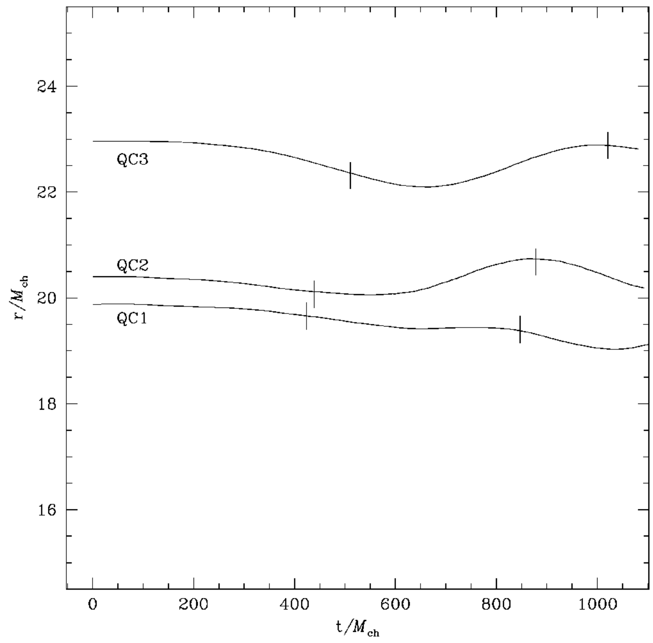

FIG. 7. Binary separation as a function of time for the binaries in runs QC1, QC2, and QC3, using initial data generated by [27], evolved forward in time with radiation reaction terms neglected. The calculations use binaries with initial separations of $r_0/\mathcal{M}_{ch} = 19.91$, 20.42, and 22.97, respectively. Full orbital periods, with $T/\mathcal{M}_{ch} = 422.8$, 438.0, and 519.7, respectively, are shown with tick marks. We see that the resulting orbits are nearly circular, with changes in separation of no more than 4% over the first two orbits. This is the strongest available evidence that the innermost point along this equilibrium sequence is actually stable against merger.

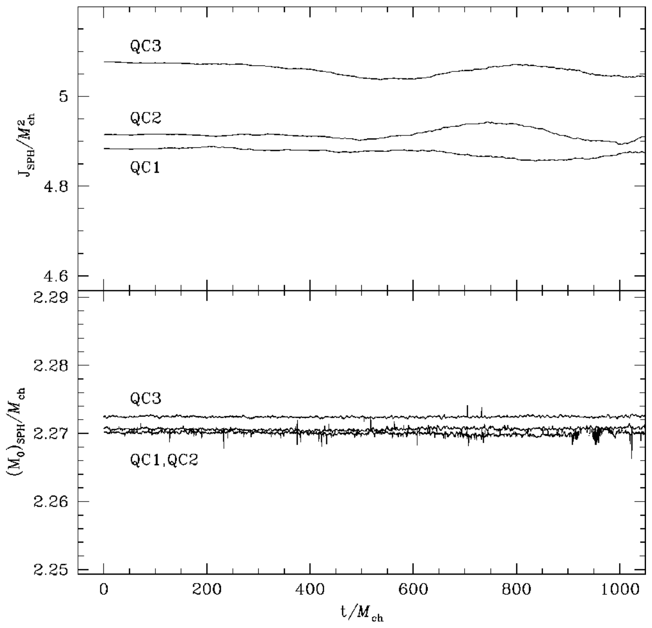

FIG. 8. ADM mass and total angular momentum, calculated from Eqs. (42) and (44), runs QC1, QC2, and QC3. We see that the ADM mass is conserved almost exactly, and the angular momentum to within 1%, with the variation occurring primarily on the orbital time scale.

irrotational sequence [55,68,69].

While this result may appear at first glance to disagree with those of [70], who find that the ISCO occurs at a greater binary separation than the termination point of an equilibrium sequence, we believe that the difference is purely semantic. We define an initial configuration to be dynamically stable if *in the absence of dissipative radiation reaction effects*, the circular orbit remains stable (no merger occurs) when evolved forward in time. In [70], a configuration is described as within the ISCO if in full GR (i.e., including dissipative radiation reaction effects), a binary starts merging (the surfaces of the two NS come into contact) *within one orbit* when evolved forward in time. Clearly, using these definitions, the same initial configuration can be dynamically stable (in the time-symmetric CF sense) at a separation within the ''ISCO'' as defined by [70].

In order to estimate how well our code respects conserved quantities, we show in Figs. 8 and 9 the evolution of both the ADM mass and system angular momentum, calculated from the SPH expressions, Eqs. (42) and (44), and the spectral basis forms, Eqs. (41) and (43), respectively. In the former, we see that the SPH expression for the ADM mass is remarkably constant over time, with only very minor deviations of relative magnitude less than a tenth of a percent. The system angular momentum varies more, but is still conserved to within 1%, with no sign of a systematic drift in either direction. We note that much of the variation is correlated with the deviations in the binary separation, oscillating on the orbital time scale. We see much more variation on an iteration to iteration basis when we look at the same quantities computed using the spectral basis. This is hardly surprising, since these

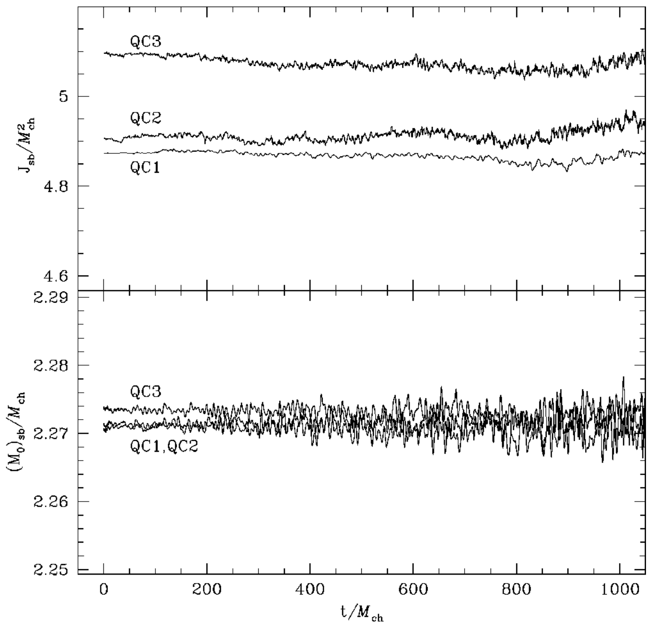

FIG. 9. ADM mass and total angular momentum, calculated in the spectral basis from Eqs. (41) and (43), for the runs shown in Fig. 7. We see roughly the same amount of variation in the angular momentum as was found for SPH summation in Fig. 8. The ADM mass shows considerably more variation than the SPH version, but remains well within 1% of the original value with no systematic drift.

values are computed at the end of a relaxation routine, and we expect some degree of variation on a step-by-step basis depending on the exact phase space path traced out by the iterative solution. All the same, we see that the angular momentum is conserved to roughly the same level in the spectral basis as it was when computed using SPH, and while the variation in the ADM mass is larger, we see no sign of a systematic drift.

V. DYNAMICAL CALCULATIONS

While dynamical calculations including the effects of radiation reaction are the only way to study the coalescence of binary NS systems, they have several additional uses which are often overlooked. Of particular importance is the ability to determine the validity of quasiequilibrium models as initial conditions for dynamical calculations, regardless of whether CF or full GR gravity is used. Thus, we computed two dynamical runs including radiation reaction. Run RR1 was started from the cusp point of the sequence (the same initial configuration used in run QC1), and was used to study the details of the coalescence process. Run RR2 was started from a larger separation (the same initial configuration used in run QC3), and was used to test out the deviations we expect from quasiequilibrium prior to reaching the termination point along the equilibrium sequence.

A. Stable regime

The evolution of the binary separation for run RR2 is shown in Fig. 10. The dotted curve, showing the result from the calculation, does not have the behavior one would expect. Notably, after the binary separation decreases monotonically until reaching $r/\mathcal{M}_{ch}=21.2$ at $t/\mathcal{M}_{ch}=700$, the system turns around and expands briefly back to a separation of $r/\mathcal{M}_{ch}=21.5$ at $t/\mathcal{M}_{ch}=950$ before shrinking again. This does not reflect any inherent problem in our radiation reaction formalism, since oscillations in the binary orbit were found for calculations which ignored all radiation reaction effects. In fact, if we ‘‘correct’’ the binary separation by looking at the difference in separation at equivalent times between runs RR2 and QC3, which were started from the same initial configuration, with and without radiation back reaction terms, we see a pattern of monotonic decrease, shown as a solid line. This seems to indicate that deviations from circularity in the orbit of the quasiequilibrium binary configurations represent a systematic effect in the evolution.

The ‘‘corrected’’ infall curve shows clear signs of an orbital eccentricity with a time scale roughly corresponding to the orbital period. This is a natural consequence of starting out from an initial condition with zero infall velocity, and has been seen before in virtually every PN and CF calculation (FR [39,48]). Its origins are clear: the framework used by GGTMB to construct quasiequilibrium initial conditions assumes a helical Killing vector exists, which enforces an initial circularity in the orbit, rather than the proper infalling trajectory. If calculations could be started from sufficiently large separations, GW emission would cause the orbit to circularize, but the process works slowly, and breaks down as the binary makes the transition toward a dynamical merger. It is fair to say that no computational scheme can currently be trusted to remain stable over the period required to circularize the orbit.

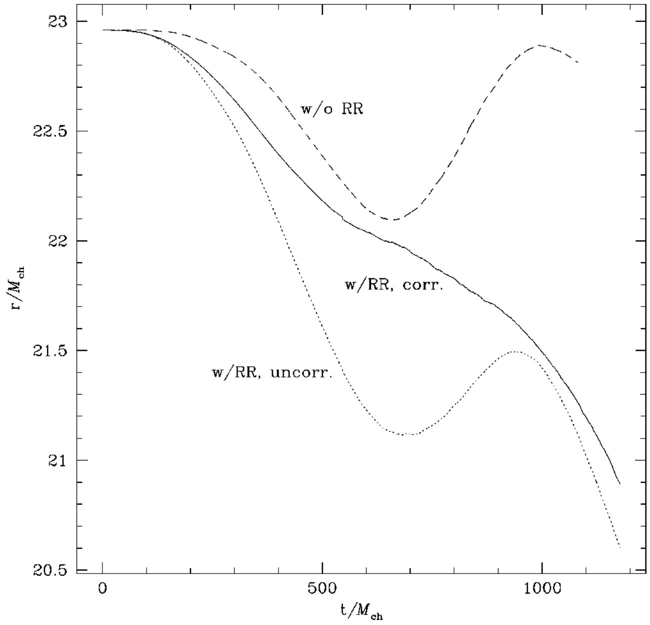

FIG. 10. Binary separation over time for run RR2, started from an initial separation of $r_0/\mathcal{M}_{ch}=22.97$, the same initial configuration that was used for run QC3. The dotted line shows the original, ‘‘uncorrected’’ result, including a separation increase from $t/\mathcal{M}_{ch}=700$–950. This is primarily due to oscillations associated with numerical noise and deviations from equilibrium in the initial configuration. Correcting for deviations from circularity in run QC3, which ignored radiation reaction (dashed curve), yields the ‘‘corrected’’ result, shown as a solid line. We see monotonic decrease in the separation over time, with an ellipticity induced by our initially circular orbit.

B. Coalescence

We have also computed the full dynamical evolution of a binary system started from the innermost point along the quasiequilibrium sequence, denoted run RR1. In Fig. 11, we show density contours from the system during the binary phase, which lasted until $t/\mathcal{M}_{ch}=883$. The contours are equally spaced logarithmically, two per decade, ranging from density values of $\mathcal{M}_{ch}^2\rho_*=10^{-6.5}-10^{-1}$. We recognize a familiar pattern from past PN and relativistic calculations (FR [39,43,48]), including the development of tidal lag angles as the time scale on which the gravitational field evolves becomes comparable to the dynamical time scale. This gives rise to an ‘‘off-axis’’ collision, as matter from the inner portion of each star runs along the trailing edge of the other, forming a turbulent vortex sheet (see FR3). Some fraction of the mass in these flows eventually crosses through the outer Lagrange point on the opposite side of the binary, forming the very low-density spiral arm structures seen at $t/\mathcal{M}_{ch}=850$. In contrast to Newtonian binaries, in which angular momentum transfer outward leads to massive spiral arm formation, the very low-density arms formed here have

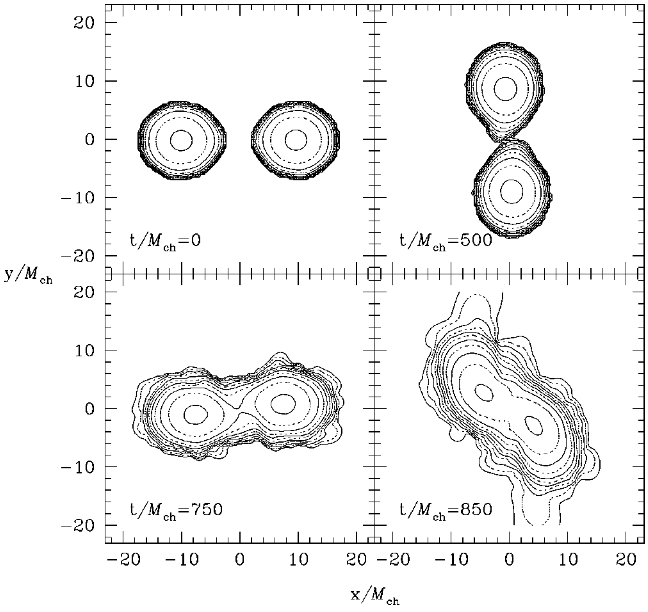

FIG. 11. The evolution of the matter run RR1, started from just outside the separation where a cusp develops. We followed the evolution through the merger and formation of a remnant. Density contours are logarithmically spaced, two per decade, ranging from $\mathcal{M}_{ch}^2\rho_* = 10^{-6.5} - 10^{-1}$. We see the development of significant tidal lag angles at $t/\mathcal{M}_{ch} = 500$, followed by an ''off-center'' collision. This process leads to the formation of a vortex sheet and a small amount of matter ejection by $t/\mathcal{M}_{ch} = 850$ from matter running along the surface of the other NS.

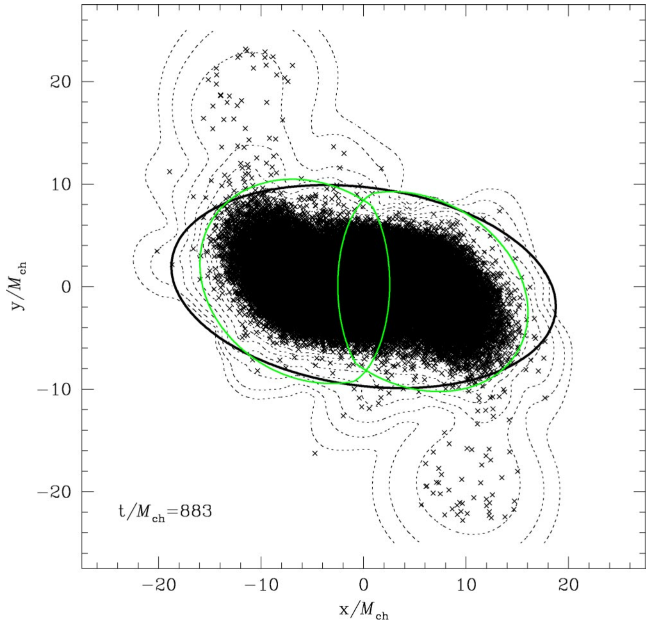

FIG. 12. Detailed view of the binary to single-star transition performed during run RR1 at $t/\mathcal{M}_{ch} = 883$. We show the positions of all SPH particles, as well as density contours, shown as dashed lines, logarithmically spaced two per decade. The surface of the inner computational domain in both the binary and single-star representations are shown as heavy solid lines, with good agreement between the two.

velocities much smaller than the escape velocity, and the vast majority of the mass remains gravitationally bound to the system.

At $t/\mathcal{M}_{ch} = 883$, shortly before the binary field solver fails to converge, we take our matter and field configurations and transform them into the single-star description described in Sec. III B. In Fig. 12, we show the particle configuration at $t/\mathcal{M}_{ch} = 883$, which can be described as a bar with two low-density arms trailing off the edges. While it may seem inappropriate at first to describe the configuration as an ellipse, we note that the low-density contours, shown as dashed lines, do form a much more elliptical pattern than one might at first expect. In interpreting SPH particle plots, it is important to remember that low-density particles have large smoothing lengths, implying that the matter distribution extends well beyond the apparent sharp edge. The boundaries of the innermost computational domains are shown in the figure as heavy solid lines, for both binary and single-star configurations. We see that they align rather well, failing to overlap only in low-density regions near the boundary. To confirm the validity of the switch, we compare the field solutions for the particles before and after the transition. In Fig. 13, we show the relative change in the lapse function N (top panel) and conformal factor A (bottom panel), as a function of the x-coordinate. We see that in all cases the relative error is $< 1\%$.

The evolution of the single-body configuration is shown in Fig. 14. We see a strong pattern of differential rotation in the merger remnant, which slowly relaxes from a very elliptical shape toward a more spheroidal one. This is to be expected, as our choice of EOS with $\Gamma = 2.0$ should not be able to support a long term ellipsoidal deformation [58]. By $t/M_{ch} = 1220$, the remnant has relaxed to a nearly circular profile, but the differential rotation, as shown in Fig. 15, persists. The latter will dissipate slowly on either the viscous or magnetic braking time scales, beyond the scope of what we can reasonably calculate [71–73]. Differential rotation is expected to stabilize the star against gravitational collapse in the short-term [74,75]. Quantitatively accurate determinations of the rotational velocity profile in terms of the parameters of the initial system are likely to be crucial for making prediction as to which systems will or will not collapse promptly to BHs, especially since these systems will likely have very large masses. As we see in Fig. 16, the vast majority of the rest mass of the system ends up in the merger remnant itself, with a fraction of a percent of the total mass forming a low-density, bound halo around the remnant. This seems to be the consensus from PN and relativistic calculations of irrotational binaries (FR3 [43]) and even PN and relativistic calculations of synchronized binaries (FR3 [48]), which traditionally yielded significantly higher mass ejection fractions in Newtonian calculations. We note that PN calculations of irrotational binaries yielded an ejected mass fraction of $\lesssim 1\%$ (FR3), rather than the 6% quoted by [43].

To compare with the relativistic results of [43,48], we show the evolution of the maximum density as a function of time in Fig. 17. We see at the earliest times a low-amplitude pulsation, resulting from small deviations from equilibrium in the initial SPH particle configuration. This pulsation

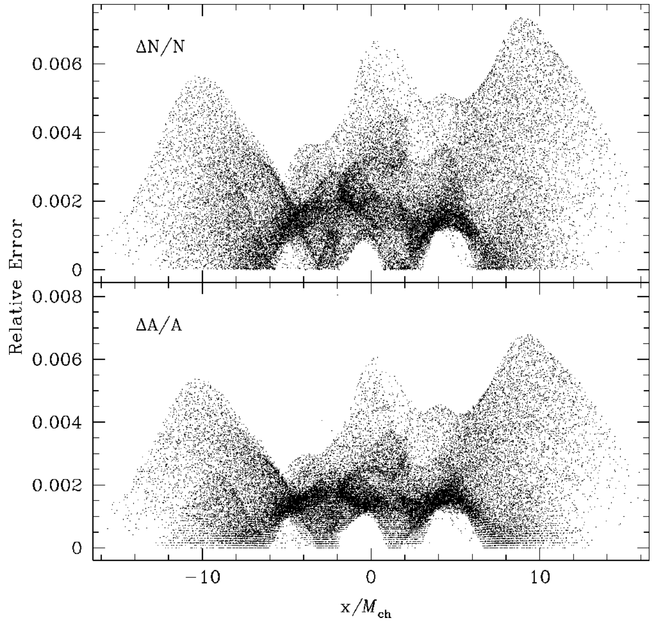

FIG. 13. The relative change in the lapse function N (top panel) and the conformal factor A immediately preceding and following the conversion from binary to single-star representations during run RR1 for every particle, shown as a function of the particle's position in the x direction. The maximum error is approximately 0.8%, with a mean difference of $\sim 0.2\%$.

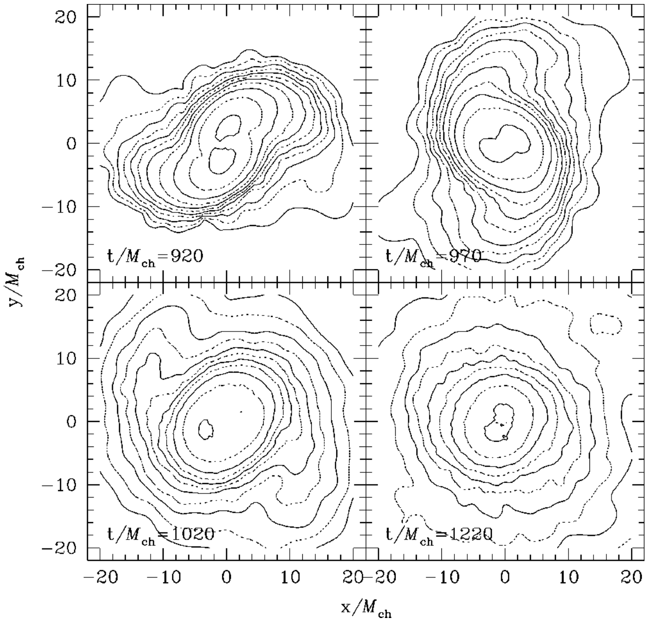

FIG. 14. The evolution of the matter in run RR1, after the transition to a single-star representation, following the same conventions Fig. 11. We see that a dense remnant forms in the center of the system, surrounded by a thin halo. Some ellipticity is seen shortly after the merger, but the system quickly relaxes toward a spheroidal configuration, with maximum density in the center of the system, unlike the toroidal configuration found by [43].

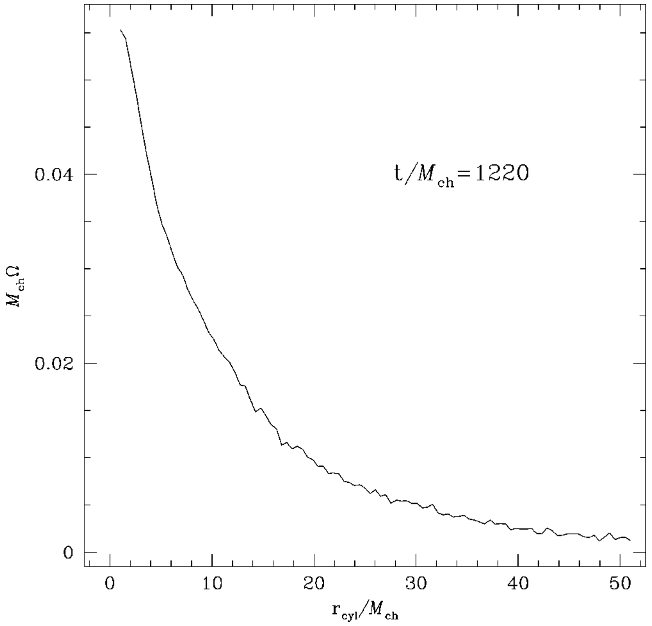

FIG. 15. Angular velocity of the merger remnant of run RR1 at $t/\mathcal{M}_{ch}=1220$, shown as a function of cylindrical radius, $r_{cyl} \equiv \sqrt{x^2+y^2}$. We see strong differential rotation, with the highest angular velocity in the center, decreasing monotonically with radius.

damps away almost completely by the time the stars plunge inward. As the system begins to accelerate rapidly inward prior to the merger itself, the maximum density decreases as the stars are tidally stretched. This effect, seen in a number of calculations, further indicates that these systems will not un-

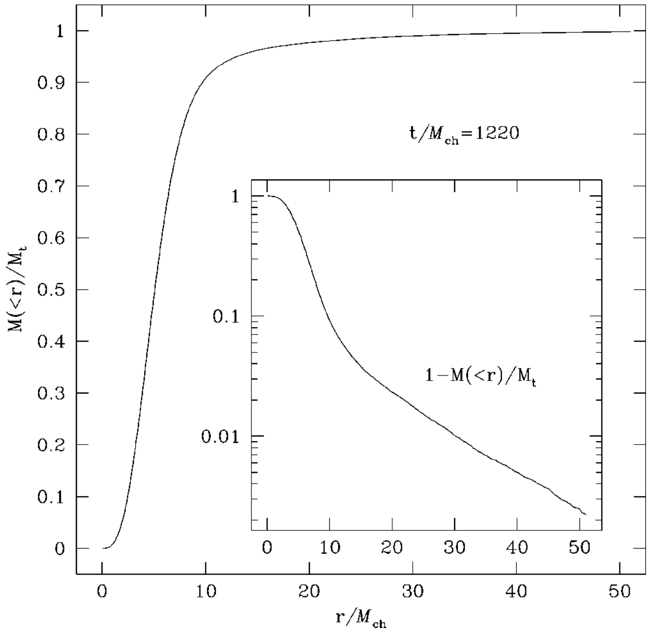

FIG. 16. Enclosed mass as a fraction of the *total* mass of the merger remnant in run RR1, at $t/\mathcal{M}_{ch}=1220$, expressed as a function of (spherical) radius. All but a few percent of the total mass of the system forms the body of the merger remnant, with no more than a small fraction of a percent ejected from the system.

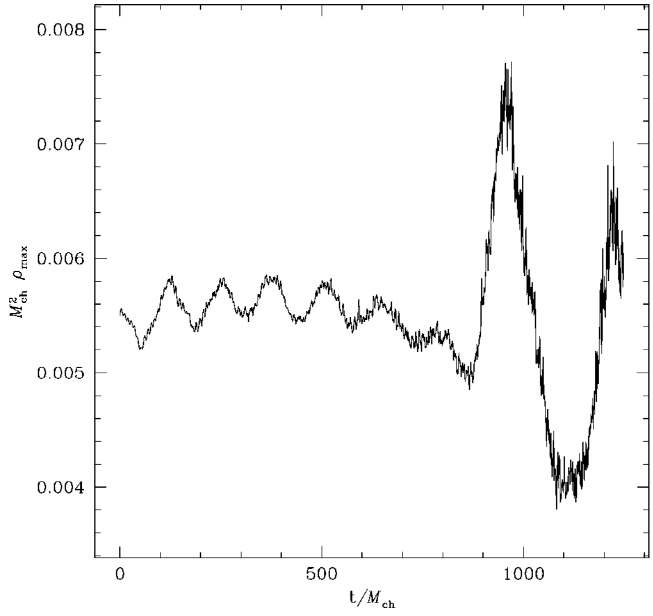

FIG. 17. Maximum density as a function of time for run RR1. We see the SPH configuration oscillates slightly around equilibrium, decreasing slowly as the binary plunges toward merger. During the merger, we see a sharp decrease, followed by a large spike upward and evidence for sharp, nonsinusoidal oscillations.

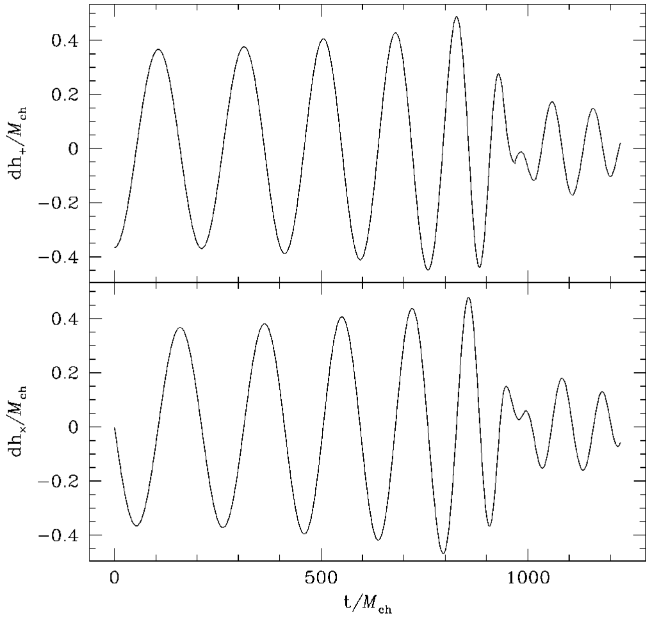

FIG. 18. The GW signal in the h_+ and $h_\times$ polarizations for run RR1, as seen by an observer situated along the vertical axis, following Eqs. (54) and (55). We see a chirp signal followed by a modulated ringdown spike. The modulation is caused by the alignment between quadrupole deformations in the inner regions of the remnant core and those at larger radius. When there is strong misalignment, there is destructive interference and the signal amplitude drops, as we see at $t/\mathcal{M}_{ch}=920$ and $t/\mathcal{M}_{ch}=1220$ in Fig. 14. At $t/\mathcal{M}_{ch}=1080$ the density contours are more aligned, and the amplitude reaches a temporary maximum.

dergo a pre-merger gravitational collapse. This process was originally suggested in [45], but is likely to have been a numerical artifact since they used a version of the CF formalism containing an error in one of the evolution equations. Indeed, the quasiequilibrium sequences in TG show a slow *decrease* in the central baryonic and energy densities, ρ_* and ρ, as the binary separation decreases. After contact, we see a strong rise in the maximum density, followed by a rapid, high-amplitude oscillation. This result is similar to that seen by [48], although they found a relatively higher maximum density value during both the peak and the trough of the oscillation. This is almost certainly a result of using different initial spin configurations. Irrotational systems, such as the one used in run RR1, concentrate relatively more angular momentum at small radii compared to initially synchronized systems, like run A of [48]. Thus, when a remnant is formed from an initially irrotational binary, the central density will typically be lower, since there is a greater centrifugal barrier and less pressure support is needed to stabilize the configuration. Our results differ rather significantly from those of [43], who found a smaller-amplitude, more sinusoidal oscillation after merger. It is possible that this discrepancy can be attributed to the use of the CF approximation rather than full GR. A much more likely explanation, however, is that the difference results from the numerical methods used to describe shock heating in the matter. Lagrangian SPH codes were used here and in [48], whereas Shibata and collaborators [41–43] use an Eulerian grid-based code, which may have a better ability to resolve shock fronts. It seems clear by examining the results from run M1414 in [43] that as the NS cores converge, the increase in the central density is suppressed by the conversion of kinetic energy into heat. The merger remnant shows a spike in the internal energy in the very center, 2–3 times the adiabatic value, and a corresponding decrease in the density, giving the remnant its toroidal profile. Only calculations using their new shock-capturing scheme [76] produce this behavior; previous calculations yielded remnants with centrally condensed density profiles [41,42]. It will be of great future interest to determine whether or not SPH studies of rapidly rotating collapsing matter configurations can produce these toroidal configurations with "hot" cores, and if so, which aspects of shock physics are crucial for understanding this process.

In Fig. 18, we show the GW signal for run RR1, calculated from Eqs. (54) and (55). The waveforms show a familiar chirp signal up until $t/\mathcal{M}_{ch}\approx 850$, followed by a modulated, high-frequency ringdown component. The strength of our signal at peak amplitude matches extremely well with the results of [43,48], as one would expect from simple dimensional analysis. Our modulated remnant signal, though, is much more similar to the results of [43] than [48], who find a damped ringdown signal of lower amplitude for this model, with no obvious modulation. Previous PN calculations (FR2, FR3) identified the source of the GW amplitude modulation as a combination of differential rotation and ellipticity in the remnant. When the inner and outer regions of the remnant have ellipsoidal deformations which are roughly aligned, as we see at $t/\mathcal{M}_{ch}\approx 900$ in Fig. 11, the GW amplitude will be at a maximum. When differential rotation drives the inner regions into misalignment, as we see at $t/\mathcal{M}_{ch}\approx 1020$ in the same figure, the GW amplitude reaches a minimum. Eventually, these effects dissipate away as the remnant relaxes toward a more spheroidal configuration. We believe the lack of modulation in the waveforms shown in Fig. 10 of [48] merely reflects the use of a different initial spin configuration. As stated above, synchronized initial configurations contain relatively less angular momentum at smaller radii, and the lack of a centrifugal barrier allows the remnant ellipticity to damp away much more quickly as the densest regions in the NS cores fall into the remnant's center. Our results are in broad agreement with those of [43], who find a modulated waveform immediately after the merger on a similar time scale as our results, before a longer-lived, smaller-amplitude damped modulation eventually appears.

Calculating the GW energy spectrum for the merger waveform is more complicated than simply applying Eq. (57), since taking the Fourier transform of a signal with nonzero initial and final values introduces aliasing of the boundary conditions into the resulting waveform. To correctly derive the proper spectrum, one must also "attach" analytic solutions to the beginning and end of the calculated signal, representing the portions of the inspiral and ringdown phases, respectively, which fall outside the bounds of the numerical evolution. In the past, the authors (FR3), and others [48,63,77], have modeled the initial inspiral phase via the Newtonian point-mass approximation, but that is clearly not physically realistic. Indeed, it has been shown in FGRT that relativistic effects should have a significant effect on the GW spectrum even before the dynamical merger. Summarized, we know that for an equal-mass binary system, the total mass-energy is given by $E=M_t-M_t^2/8r^2=2^{1.2}\mathcal{M}_{ch}-\mathcal{M}_{ch}^2/(2^{0.6}r^2)$, and the (Keplerian) orbital frequency by $f_{Kep}=(\sqrt{M_t/r^3})/2\pi$. In terms of the GW emission frequency, $f_{GW}\equiv 2f_{Kep}=(2^{0.6}/\pi)\sqrt{\mathcal{M}_{ch}/r^3}$, we find

$$E_N(f_{GW})=2^{1.2}\mathcal{M}_{ch}-\frac{\pi^{2/3}}{2}\mathcal{M}_{ch}^{5/3}f_{GW}^{2/3}, \tag{90}$$

$$\frac{dE_N}{df_{GW}}=\frac{\pi^{2/3}}{3}\mathcal{M}_{ch}^{5/3}f_{GW}^{-1/3}, \tag{91}$$

where the latter equation demonstrates the familiar power-law dependence of the GW energy spectrum.

For the quasiequilibrium sequence from which we take our initial condition, we found that the system ADM mass can be given in terms of the GW frequency by a (phenomenological) fit of the form

$$E(f_{GW})/\mathcal{M}_{ch}=E_N/\mathcal{M}_{ch}-0.4905(\mathcal{M}_{ch}f_{GW}) \\ +231(\mathcal{M}_{ch}f_{GW})^2. \tag{92}$$

Differentiating this equation yields what we term the "quasiequilibrium energy spectrum," but we require additional assumptions to be made before we can construct the time history of the inspiral waveform. First, we determine a fit for the GW frequency as a function of conformal separation, finding that we can approximate the proper function to within 0.1% with the form

$$\mathcal{M}_{ch}f_{GW}=\frac{2^{0.6}}{\pi}(r/\mathcal{M}_{ch})^{-1.5}-1.592(r/\mathcal{M}_{ch})^{-2.5} \\ +6.325(r/\mathcal{M}_{ch})^{-3.5}. \tag{93}$$

Next, we assume that the GW signal amplitude is given by a slightly modified version of the quadrupole form,

$$Q_{xx}^{[2]}(t)=-Q_{yy}^{[2]}(t) \\ =(1.0-\kappa)2^{0.2}\pi^2\mathcal{M}_{ch}r^2f_{GW}^2\cos(\theta_{GW}(t)), \tag{94}$$

$$Q_{xy}^{[2]}(t)=(1.0-\kappa)2^{0.2}\pi^2\mathcal{M}_{ch}r^2f_{GW}^2 \\ \times\sin(\theta_{GW}(t)), \tag{95}$$

where the prefactor κ is used to match the amplitude of the inspiral signal onto that at the beginning of our calculated signal. We find that $\kappa=0.015$ throughout the early phases of our calculated waveform, indicating that it can be well-approximated by the expected quadrupole form. Furthermore, we note that the resulting energy spectrum is essentially independent of κ; as κ increases, the GW amplitude decreases, decreasing both the energy loss rate and the frequency sweep rate in the same proportion, leaving dE/df unchanged. Finally, we assume that the energy loss rate in GWs is given by the standard quadrupole expression,

$$dE/dt=0.2\langle 4\pi^2f_{GW}^2Q_{ij}^{[2]}Q_{ij}^{[2]}\rangle. \tag{96}$$

To construct the inspiral waveform, we start from a point along our calculated waveform and evolve backward in time from that point. At every time step, we calculate the instantaneous energy loss rate from Eq. (96). After adjusting the total energy, we calculate the new GW frequency by implicitly solving Eq. (92), and adjust the phase of the GW signal appropriately. We find the new binary separation by solving Eq. (93) implicitly, and finally evaluate the waveform via Eqs. (94) and (95).

The question of where to match the quasiequilibrium waveform to the calculated one deserves some attention. Matching the two at $t=0$ is very much a mistake, because it represents a transition from an infalling configuration to a circular one; beforehand, the frequency sweep rate df_{GW}/dt is positive and increasing, while afterward it is reset instantaneously to zero. This mismatch in the infall velocity, and thus the frequency sweep rate, results in energy "piling up" at the transition frequency, as can be seen in FR3 and to a smaller degree in Fig. 12 of [48]. We find that matching the inspiral waveform to the calculated signal at $t=0$ reproduces this error, but that by $t/\mathcal{M}_{ch}=250$, the match in the inspiral velocity is sufficient to leave no measurable trace in the resulting spectrum.

We note that [48] also match their inspiral waveform to their calculated one at some time into the calculation, but we believe that they place too much trust in the behavior of the energy spectrum near this transition frequency. In their paper, they alter the frequency of a Newtonian inspiral waveform to match their relativistic calculation by adjusting by hand the coalescence time, $\tau\equiv(dr/dt)/r$. We believe this approach to be a mistake. The effect of this change is to use a Newtonian waveform with different physical parameters from those used in the calculation; in particular, it is equivalent to calculating a Newtonian waveform using the wrong *total mass*, and thus the wrong limit for the spectrum at low frequencies. It is only through the use of an inspiral waveform whose frequency approaches the proper Keplerian limit at low frequencies and the *relativistic* form at high frequencies that accurate energy spectra can be constructed. Indeed, since our initial condition was taken from the same quasiequilibrium sequence used to generate our frequency data, the initial GW frequency derived from our calculation matched that of the inspiral waveform within 0.1% without requiring further manipulation.

In Fig. 19, we show as a solid line what we believe to be the first complete and consistent relativistic waveform for a binary NS merger at frequencies $f_{GW} \leqslant 1.5$ kHz. The frequencies listed on the upper axis assume our "standard model" parameters, i.e., each NS has an ADM mass $M_0 = 1.4 M_\odot$. The two dotted lines show the components which make up the energy spectrum. At low frequencies, $\mathcal{M}_{ch} f_{GW} < 0.004$, we see the primary contribution is from the quasiequilibrium inspiral waveform, whereas at higher frequencies it is from our calculated waveform. The short-dashed line shows the Newtonian point-mass relation, given by Eq. (91), and the long-dashed curve the quasiequilibrium result, found by numerically differentiating Eq. (92). We see excellent agreement between our calculated waveform and the quasiequilibrium fit, up until frequencies $\mathcal{M}_{ch} f_{GW} \approx 0.007 - 0.009$. This peak represents the "piling up" of energy at the frequency corresponding to the phase of maximum GW luminosity, as the stars make contact and the infall rate drops dramatically. The second peak, at $\mathcal{M}_{ch} f_{GW} \approx 0.010 - 0.011$, represents emission from the ringdown of the merger remnant. It is likely that we underestimate the true height of this second peak, since we assume that the GW signal after our calculation damps away exponentially. Still, it is extremely unlikely that including the ringdown phase will increase the strength of this peak by more than a factor of a few, since our chosen EOS will not support a long-lived ellipsoidal deformation, and it is likely that the ringdown oscillations will smear the GW emission over a small range of frequencies rather than coherently emitting at a single frequency.

In general, the energy spectrum we calculated here confirms the general conclusions we put forward in FR3 and FGRT, albeit in a much more consistent way. The GW energy spectrum does show a significant drop away from the Newtonian point-mass form at frequencies significantly below 1 kHz, in almost the exact same form as we predicted from quasiequilibrium data alone in FGRT. Nowhere does the spectrum rise above the Newtonian value, including the peaks associated with maximum GW luminosity and the ringdown oscillations. These results suggest that the weak signal amplitude of the peaks above 1 kHz, which lie outside the Advanced LIGO broadband frequency range, may inhibit detections by high-frequency narrow-band interferometers as well. However, combining lower-frequency narrow-band detectors with broadband LIGO measurements, as suggested in [34], appears extremely feasible, and may allow GW measurements to constrain the NS compactness and EOS.

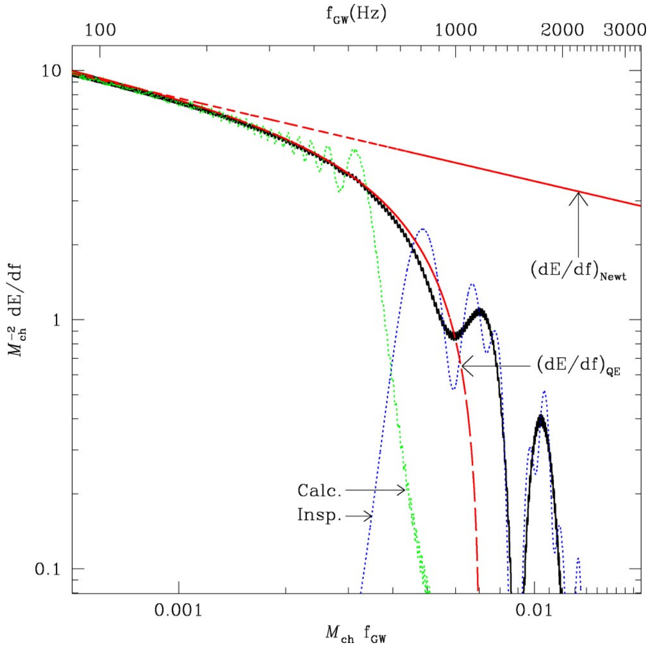

FIG. 19. GW energy spectrum, $\mathcal{M}_{ch}^{-2} dE/df$, as a function of the GW frequency, $\mathcal{M}_{ch} f_{GW}$, for run RR1. The dotted lines show, respectively at high and low frequencies, the components contributed by our calculated signal and the quasiequilibrium inspiral component. Also shown are the Newtonian point-mass energy spectrum $(dE/df_{GW})_{Newt}$ (short-dashed line), Eq. (91), and the quasiequilibrium fit $(dE/df_{GW})_{QE}$ derived from Eq. (92). We see confirmation that the "break frequency" calculated from a fit of $E(f)$ for the equilibrium sequence (i.e., the frequency at which the energy spectrum decreases to a given fraction of the Newtonian level) is reproduced by a full numerical evolution. On the upper axis, we show the corresponding frequencies in Hz assuming the NS each have a mass $M_0 = 1.4 M_\odot$ The two peaks correspond to the phases of maximum GW luminosity and ringdown oscillations, respectively.

One possible cause for concern with our code is nonconservative behavior caused by numerical errors that develop after $t/\mathcal{M}_{ch} = 500$. In Fig. 20, we show the change in the system's angular momentum over time. The dotted curve is the uncorrected result derived from our calculation, which shows two periods of angular momentum generation, the first from $t/\mathcal{M}_{ch} = 600 - 700$, and the second at $t/\mathcal{M}_{ch} = 875 - 900$. The former is associated with the numerical inaccuracies discussed in Sec. V A for run RR2. All of our runs show some spurious angular momentum generation and slowing of the binary infall during this period. The latter spike occurs immediately before and after the transition from a binary to a single-star description. Correcting for both of these spurious terms yields the solid line on the plot, which still underestimates by a nontrivial amount the angular momentum loss we would expect from the quadrupole formula,

$$(\dot{J}_k)_{GW} = 0.4 \epsilon_{ijk} \langle Q_{il}^{[2]} Q_{lk}^{[3]} \rangle. \tag{97}$$

Using the quadrupole formula on our results yields a total angular momentum loss fraction which very nearly equals

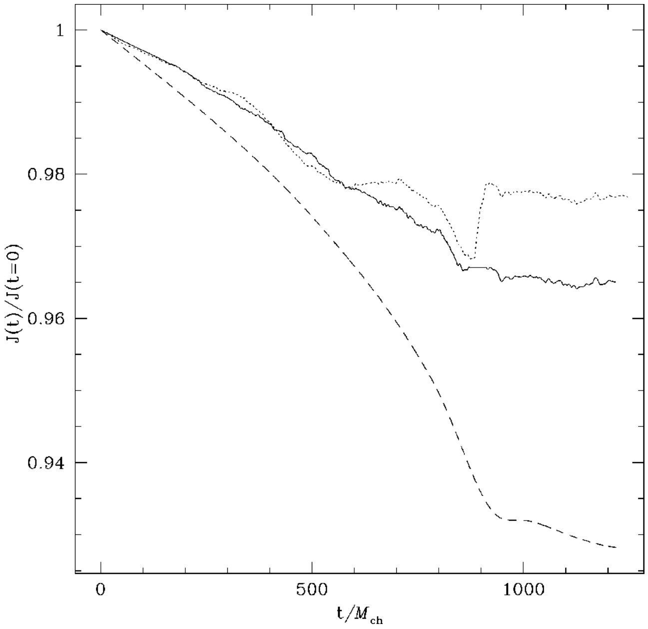

FIG. 20. Angular momentum loss for the binary in run RR1 measured using the SPH integral, Eq. (44) (dotted line), and the result after correcting for spurious angular momentum creation during the binary to single-object transition (solid line). We see that the result yields an angular momentum loss approximately half that we would have predicted from the quadrupole formula, Eq. (97) (dashed line), primarily because our estimate for the system's angular velocity used in the back reaction force is systematically lower than the GW signal would indicate. The quadrupole result we derive shows that about 7% of the system angular momentum is emitted in GWs, in line with previous relativistic estimates.

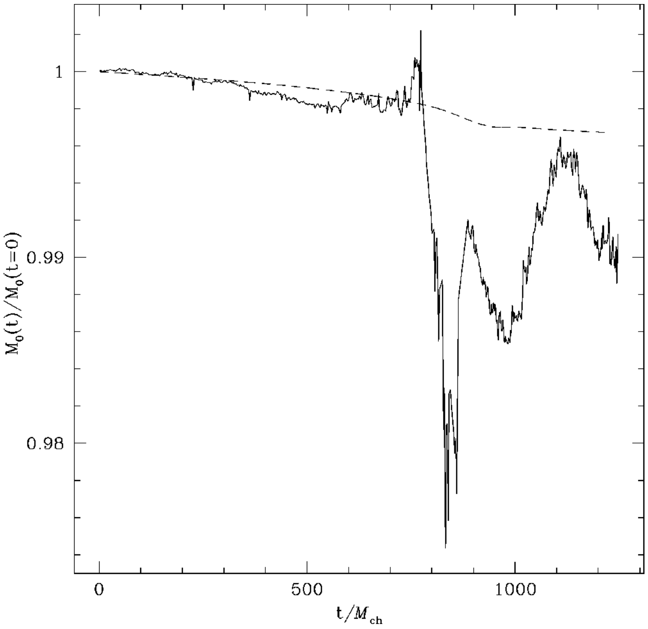

FIG. 21. The evolution of the total ADM mass for the system in run RR1, calculated using the SPH integral, Eq. (42) (solid line). Up until $t/\mathcal{M}_{ch}=600$, we see a slow decrease as energy is emitted in GWs, at approximately the rate predicted by the quadrupole formula, Eq. (96) (dashed line). Beyond $t/\mathcal{M}_{ch}=600$ numerical inaccuracies lead to oscillations of total amplitude $\sim 2\%$. From the quadrupole estimate, we find that 0.4% of the system's energy is radiated away as GWs, in line with previous estimated from relativistic calculations.

that found by [43,48], with approximately 7% of the system's angular momentum converted into GW emission. The discrepancy between this amount and what we derive from the SPH particle configuration, Eq. (44), can be easily understood. First, we do not see strong angular momentum loss as the NS first make contact, since this is where we push our field solver to its limit. Second, our method for estimating the instantaneous angular velocity, Eq. (53), underestimates the proper value of ω, yielding a radiation reaction force, Eq. (45), smaller than the correct quadrupole value (which we can determine after the fact). This error could be decreased in magnitude by calculating the angular velocity from the change of position of the NS centers-of-mass in time, but such a prescription is difficult to define consistently in the single-body regime. Even defining the orbital frequency in terms of the rate of change of the quadrupole tensor, as done by [48], underestimates the correct angular momentum loss rate by up to 40% during the GW emission peak.

We see a similar pattern at work in the evolution of the system's ADM mass, shown in Fig. 21, comparing the energy loss to GWs from the quadrupole approximation formula (dashed line), Eq. (96), to the value we find from SPH summation via Eq. (42) (solid line). The quadrupole value agrees well with other calculations, which typically find $\Delta M_{ADM}/M_{ADM}=0.004$. Looking at our particle summation value, we see a slow decrease from $t/\mathcal{M}_{ch}=0$–500, of magnitude 0.2–0.3 % of total value, in good agreement with other calculations and our own quadrupole estimate. From that point on, we see a small spurious increase from the point the numerical errors begin to become significant, followed by a sharp decrease of $\sim 2\%$ immediately prior to our transition from binary to single-star descriptions. Once we have made the transition, the ADM mass oscillates slightly, with an overall peak-to-trough amplitude of 1%. Thus, we conclude that while the instantaneous value we measure from the particles directly is liable to be off by up to 2%, we can reconstruct the proper energy loss rate after the calculation is over.

VI. CONCLUSIONS

We have developed and tested a new relativistic 3D Lagrangian hydrodynamics code, which should prove useful for studying a wide variety of physical systems. Here, as an initial investigation, we have performed the first full evolutions of the coalescence and merger of irrotational binary NS in the CF approximation to GR. Moreover, these calculations represent the first numerical evolution of coalescing binary systems performed with either a spectral methods field solver or the use of spherical coordinates adapted to a binary environment.

The code has been validated using several tests. We can accurately reproduce static spherical stellar configurations as well as the known solution for a collapsing pressureless dust cloud. In both cases, the CF approximation yields the exact solution in GR, as it will for any spherical configuration. We find that we can reproduce these known semianalytic solutions to high accuracy, up until the formation of an event horizon for the collapsing dust clouds.

Our dynamical evolution calculations for quasiequilibrium models at a number of different binary separations indicates that we can successfully integrate forward for several orbits, with typical errors in conserved quantities of $\sim 1\%$. In doing so, we have demonstrated directly for the first time that the $M/R = 0.14$, equal-mass sequence of TG is stable all the way to its innermost configuration, at which point a cusp develops on the inner edge of each NS.

Our dynamical calculation of a complete binary NS merger, including radiation reaction effects, demonstrated that our spherical coordinates, spectral method approach is robust enough to follow the system from the point just before the formation of a cusp through merger and the formation of a stable remnant. Some errors were introduced during this period into the globally conserved quantities such as the ADM mass and system angular momentum, but we find that the field values were computed consistently throughout, and that the global dynamics was treated in a quantitatively accurate way.

We find that the merger remnant formed in our calculation is differentially rotating, with a transient quadrupole deformation. This combination of effects produces a GW amplitude with a modulated form, similar to what has been seen before in PN calculations (FR3) and more recent full GR calculations of the same model [43]. We find that the remnant is initially stable against gravitational collapse, as did [43], with the supermassive NS (which has a baryonic mass essentially twice that of either NS in isolation) supported by strong differential rotation. We find that a density maximum develops rather rapidly in the center of the merger remnant, as has been seen in all other PN and CF calculations, but not that of [43], whose full GR merger calculation yielded a toroidal remnant. We believe the difference results from their use of a capturing scheme, whereas our runs were performed using an adiabatic treatment.

By combining our calculated GW signal with a relativistic quasiequilibrium inspiral precursor, we have generated the first GW energy spectrum from a binary NS merger which is complete at all sub-kHz frequencies and consistent throughout. We find that the energy spectrum deviates from the Newtonian power-law relation by more than 50% at frequencies $f_{GW} < 1$ kHz (the ‘‘break frequency’’), in very good agreement with the predictions of FGRT. There are distinct peaks in the power spectrum corresponding to the phases of maximum GW luminosity and merger remnant ringdown, but at levels significantly below the point-mass power-law value.

In our future work on binary NS systems, we hope to address a number of topics, many of which deserve much more careful study. Based on the excellent agreement between our calculated GW energy spectrum and that based purely on equilibrium sequence data, we hope to do a broad phase space survey to determine the dependence of the ‘‘break frequency’’ on both the NS EOS and the system's mass ratio. Beyond this parameter study of NS-NS mergers, we also plan to investigate in detail the formation process for the merger remnant, to determine the conditions which may lead to the formation of a quasitoroidal merger remnant. This will necessarily involve the use of a relativistic artificial viscosity scheme to treat shocks. The density profile of the merger remnant is likely to influence the final fate of the system, and may prove crucial for determining the coincidence properties of GW emissions and short-period GRBs, should they result from compact object binary mergers, as has been widely suggested.

ACKNOWLEDGMENT

This work was supported by NSF grants PHY-0133425 and PHY-0245028 to Northwestern University.

[1] LIGO Science Collaboration, G. González, Class. Quantum Grav. **21**, S691 (2004).

[2] LIGO Science Collaboration, G. González, ArXiv General Relativity and Quantum Cosmology reports, gr-qc/0303117.

[3] See also http://www.ligo.org

[4] M. Hewitson, P. Aufmuth, C. Aulbert, S. Babak, and R. Balasubramanian, Class. Quantum Grav. **20**, 581 (2003).

[5] See also http://www.geo600.uni-hannover.de

[6] TAMA Collaboration, M. Ando, Class. Quantum Grav. **19**, 1409 (2002).

[7] See also http://tamago.mtk.nao.ac.jp

[8] A. Giazotto and S. Braccini, in *Recent Developments in General Relativity*, 14th SIGRAV Conference on General Relativity and Gravitational Physics, Genova, Italy, 2000, edited by R. Cianci, R. Collina, M. Francaviglia, and P. Fré (Springer, Milano, 2002), pp. 111–119.

[9] VIRGO Collaboration, F. Acernese, Class. Quantum Grav. **21**, 385 (2004).

[10] See also http://www.virgo.infn.it

[11] K. Belczynski, V. Kalogera, and T. Bulik, Astrophys. J. **572**, 407 (2002).

[12] M. Burgay *et al.*, Nature (London) **426**, 531 (2003).

[13] C. Kim, V. Kalogera, and D.R. Lorimer, Astrophys. J. **584**, 985 (2003).

[14] V. Kalogera *et al.*, Astrophys. J. Lett. **601**, L179 (2004).

[15] R.A. Hulse and J.H. Taylor, Astrophys. J. Lett. **195**, L51 (1975).

[16] J.H. Taylor, A. Wolszczan, T. Damour, and J.M. Weisberg, Nature (London) **355**, 132 (1992).

[17] J. M. Weisberg and J. H. Taylor, in *Radio Pulsars*, ASP Conf. Ser. No. 302, edited by M. Bailes, D.J. Nice, and S.E. Thorsett (ASP, San Francisco, 2003), pp. 93–98.

[18] L. Blanchet, Living Rev. Relativ. **5**, 3 (2002).

[19] T. Damour, B.R. Iyer, and B.S. Sathyaprakash, Phys. Rev. D **62**, 084036 (2000).

[20] T. Damour, B.R. Iyer, and B.S. Sathyaprakash, Phys. Rev. D **66**, 027502 (2002).

[21] L.E. Kidder, Phys. Rev. D **52**, 821 (1995).

[22] T.A. Apostolatos, C. Cutler, G.J. Sussman, and K.S. Thorne, Phys. Rev. D **49**, 6274 (1994).

[23] T.A. Apostolatos, Phys. Rev. D **52**, 605 (1995).

[24] F.A. Rasio and S.L. Shapiro, Class. Quantum Grav. **16**, 1 (1999).

[25] S. Bonazzola, E. Gourgoulhon, and J. Marck, Phys. Rev. Lett. **82**, 892 (1999).

[26] E. Gourgoulhon, P. Grandclément, K. Taniguchi, J. Marck, and S. Bonazzola, Phys. Rev. D **63**, 064029 (2001).

[27] K. Taniguchi and E. Gourgoulhon, Phys. Rev. D **66**, 104019 (2002).

[28] T.W. Baumgarte, G.B. Cook, M.A. Scheel, S.L. Shapiro, and S.A. Teukolsky, Phys. Rev. Lett. **79**, 1182 (1997).

[29] T.W. Baumgarte, G.B. Cook, M.A. Scheel, S.L. Shapiro, and S.A. Teukolsky, Phys. Rev. D **57**, 7299 (1998).

[30] P. Marronetti, G.J. Mathews, and J.R. Wilson, Phys. Rev. D **60**, 087301 (1999).

[31] K. Uryū and Y. Eriguchi, Phys. Rev. D **61**, 124023 (2000).

[32] K. Uryū, M. Shibata, and Y. Eriguchi, Phys. Rev. D **62**, 104015 (2000).

[33] J.A. Faber, P. Grandclément, F.A. Rasio, and K. Taniguchi, Phys. Rev. Lett. **89**, 231102 (2002).

[34] S.A. Hughes, Phys. Rev. D **66**, 102001 (2002).

[35] J.A. Faber and F.A. Rasio, Phys. Rev. D **65**, 084042 (2002).

[36] J.A. Faber and F.A. Rasio, Phys. Rev. D **62**, 064012 (2000).

[37] J.A. Faber, F.A. Rasio, and J.B. Manor, Phys. Rev. D **63**, 044012 (2001).

[38] M. Shibata, K. Oohara, and T. Nakamura, Prog. Theor. Phys. **98**, 1081 (1997).

[39] S. Ayal, T. Piran, R. Oechslin, M.B. Davies, and S. Rosswog, Astrophys. J. **550**, 846 (2001).

[40] L. Blanchet, T. Damour, and G. Schaefer, Mon. Not. R. Astron. Soc. **242**, 289 (1990).

[41] M. Shibata and K. Uryū, Phys. Rev. D **61**, 064001 (2000).

[42] M. Shibata and K. Uryū, Prog. Theor. Phys. **107**, 265 (2002).

[43] M. Shibata, K. Taniguchi, and K. Uryu, Phys. Rev. D **68**, 084020 (2003).

[44] J. A. Isenberg, report, University of Maryland, 1978 (unpublished).

[45] J.R. Wilson, G.J. Mathews, and P. Marronetti, Phys. Rev. D **54**, 1317 (1996).

[46] É.É. Flanagan, Phys. Rev. Lett. **82**, 1354 (1999).

[47] M. Shibata, T.W. Baumgarte, and S.L. Shapiro, Phys. Rev. D **58**, 023002 (1998).

[48] R. Oechslin, S. Rosswog, and F. Thielemann, Phys. Rev. D **65**, 103005 (2002).

[49] L. Bildsten and C. Cutler, Astrophys. J. **400**, 175 (1992).

[50] C.S. Kochanek, Astrophys. J. **398**, 234 (1992).

[51] S. Bonazzola, E. Gourgoulhon, and J. Marck, Phys. Rev. D **58**, 104020 (1998).

[52] P. Grandclément, S. Bonazzola, E. Gourgoulhon, and J.-A. Marck, J. Comput. Phys. **170**, 231 (2001).

[53] K. Taniguchi, E. Gourgoulhon, and S. Bonazzola, Phys. Rev. D **64**, 064012 (2001).

[54] K. Taniguchi and E. Gourgoulhon, Phys. Rev. D **65**, 044027 (2002).

[55] K. Taniguchi and E. Gourgoulhon, Phys. Rev. D **68**, 124025 (2003).

[56] G.J. Mathews, P. Marronetti, and J.R. Wilson, Phys. Rev. D **58**, 043003 (1998).

[57] C. Cutler and É.E. Flanagan, Phys. Rev. D **49**, 2658 (1994).

[58] F.A. Rasio and S.L. Shapiro, Astrophys. J. **401**, 226 (1992).

[59] Many of the computational details described here are extensively documented in the online manual accompanying our publicly released Newtonian SPH code; for more details, see http://www.astro.northwestern.edu/StarCrash

[60] J.C. Lombardi, A. Sills, F.A. Rasio, and S.L. Shapiro, J. Comput. Phys. **152**, 687 (1999).

[61] F.A. Rasio and J.C. Lombardi, J. Comput. Appl. Math. **109**, 213 (1999).

[62] J.J. Monaghan and J.C. Lattanzio, Astron. Astrophys. **149**, 135 (1985).

[63] X. Zhuge, J.M. Centrella, and S.L.W. McMillan, Phys. Rev. D **50**, 6247 (1994).

[64] C. W. Misner, K. S. Thorne, and J. A. Wheeler, *Gravitation* (Freeman, San Francisco, 1973).

[65] K.D. Kokkotas and J. Ruoff, Astron. Astrophys. **366**, 565 (2001).

[66] L.I. Petrich, S.L. Shapiro, and S.A. Teukolsky, Phys. Rev. D **31**, 2459 (1985).

[67] L.I. Petrich, S.L. Shapiro, and S.A. Teukolsky, Phys. Rev. D **33**, 2100 (1986).

[68] D. Lai, F.A. Rasio, and S.L. Shapiro, Astrophys. J., Suppl. Ser. **88**, 205 (1993).

[69] J.C. Lombardi, F.A. Rasio, and S.L. Shapiro, Phys. Rev. D **56**, 3416 (1997).

[70] P. Marronetti, M.D. Duez, S.L. Shapiro, and T.W. Baumgarte, Phys. Rev. Lett. **92**, 141101 (2004).

[71] S.L. Shapiro, Astrophys. J. **544**, 397 (2000).

[72] J.N. Cook, S.L. Shapiro, and B.C. Stephens, Astrophys. J. **599**, 1272 (2003).

[73] Y.T. Liu and S.L. Shapiro, Phys. Rev. D **69**, 044009 (2004).

[74] T.W. Baumgarte, S.L. Shapiro, and M. Shibata, Astrophys. J. Lett. **528**, L29 (2000).

[75] N.D. Lyford, T.W. Baumgarte, and S.L. Shapiro, Astrophys. J. **583**, 410 (2003).

[76] M. Shibata, Phys. Rev. D **67**, 024033 (2003).

[77] X. Zhuge, J.M. Centrella, and S.L.W. McMillan, Phys. Rev. D **54**, 7261 (1996).